ARTICLE

doi:10.1038/nature15710

Combinatorial gene regulation by modulation of relative pulse timing

Yihan Lin[1,2], Chang Ho Sohn[3], Chiraj K. Dalal[1,2]†, Long Cai[3] & Michael B. Elowitz[1,2]

Studies of individual living cells have revealed that many transcription factors activate in dynamic, and often stochastic, pulses within the same cell. However, it has remained unclear whether cells might exploit the dynamic interaction of these pulses to control gene expression. Here, using quantitative single-cell time-lapse imaging of *Saccharomyces cerevisiae*, we show that the pulsatile transcription factors Msn2 and Mig1 combinatorially regulate their target genes through modulation of their relative pulse timing. The activator Msn2 and repressor Mig1 showed pulsed activation in either a temporally overlapping or non-overlapping manner during their transient response to different inputs, with only the non-overlapping dynamics efficiently activating target gene expression. Similarly, under constant environmental conditions, where Msn2 and Mig1 exhibit sporadic pulsing, glucose concentration modulated the temporal overlap between pulses of the two factors. Together, these results reveal a time-based mode of combinatorial gene regulation. Regulation through relative signal timing is common in engineering and neurobiology, and these results suggest that it could also function broadly within the signalling and regulatory systems of the cell.

In order to respond to environmental conditions, cells make extensive use of combinatorial gene regulation, in which two or more transcription factors co-regulate common target genes. Most analysis of combinatorial regulation presumes that the concentrations of transcription factors in the nucleus are regulated in a continuous (non-pulsatile) manner[1,2]. However, recent work has identified a large and growing list of transcription factors that activate in pulses[3–11]. In such systems, a single pulse begins when many molecules of a given transcription factor are activated simultaneously, and ends when they are deactivated. Such pulses can occur repetitively, even under constant conditions. Pulsatile regulation has been observed in bacteria[9,12,13], yeast[8,10,14–17], and mammalian stress response and signalling pathways[6,7,11,18–23]. In these systems, inputs typically modulate the pulse frequency, amplitude, and/or duration of individual transcription factors to regulate genes. However, despite analysis of many individual pulsatile transcription factors, the interactions between multiple pulsatile systems in the same cell have not yet been explored and analysed.

Saccharomyces cerevisiae provides an ideal model system to analyse such dynamic transcription factor interactions. It contains several well-characterized pulsatile systems that control core cellular functions. In particular, the general stress response transcription factor Msn2, and its paralogue, Msn4, activate hundreds of target genes in response to diverse stresses including ethanol, heat, oxidative stress, salt, and glucose starvation[24–30]. Similarly, the repressor Mig1, along with its paralogue, Mig2, control many target genes, especially those involved in metabolism, in response to changes in glucose concentration[31–33]. Together, Msn2 and Mig1 co-regulate over 300 target genes (according to Yeastract[34]). Both Msn2 and Mig1 are activated by dephosphorylation, which leads to nuclear localization[35–37]. Previous work has shown that Msn2 nuclear localization can occur in a pulsatile fashion in response to various inputs[8,10,14,17,38]. Mig1 is known to quickly localize to the nucleus in response to an increase in glucose levels[36], and can also exhibit pulsatile activation[38].

Two stages of dynamic pulsing

To analyse Msn2 and Mig1 dynamics in the same cell, we constructed strains expressing fusions of Msn2 and Mig1 proteins to the distinguishable fluorescent proteins[39] mKO2 and mCherry, respectively (Fig. 1a). To simplify the analysis, we knocked out their paralogues Msn4 and Mig2 (Methods). We attached single cells to the glass surface of a microfluidic channel, maintaining a constant flow of media, while acquiring time-lapse movies. By analysing individual cells in these movies, we could track the nuclear localization dynamics of both proteins over time (Methods).

We first analysed the effects of glucose reduction, which is known to induce changes in nuclear localization for both transcription factors[35,36]. In response to a sudden step from 0.2% to 0.1% glucose, both proteins exhibited pulses of nuclear localization, but did so with different timing (Fig. 1b). Msn2 localized to the nucleus immediately, while Mig1 exited the nucleus. Subsequently, in many cells (75%), Msn2 exited the nucleus followed by the re-entry of Mig1 (Fig. 1b; Supplementary Video 1). This transient response terminated within ~30 min (Fig. 1b, bottom). We describe events like this, in which Msn2 and Mig1 pulses are temporally separated, as non-overlapping (see Fig. 1b, top and Methods). After this event, Msn2 and Mig1 exhibited sporadic pulsing that was unsynchronized between cells (Supplementary Video 1). During this steady-state period, we observed both overlapping (that is, coincident) events, in which Msn2 and Mig1 pulses overlap, as well as non-overlapping events in which Msn2, but not Mig1 localized to the nucleus (Fig. 1b, top and Methods).

These data provoke two interrelated questions about whether and how relative pulse timing could function in combinatorial regulation (Fig. 1c): first, do inputs modulate the relative timing of transcription factor pulses, either during the transient response to a change in conditions, or during the subsequent period of repetitive pulsing? Second, if so, how does such pulse timing modulation affect downstream combinatorial gene regulation?

[1]Howard Hughes Medical Institute, California Institute of Technology, Pasadena, California 91125, USA. [2]Division of Biology and Biological Engineering, California Institute of Technology, Pasadena, California 91125, USA. [3]Division of Chemistry and Chemical Engineering, California Institute of Technology, Pasadena, California 91125, USA. †Present address: Department of Microbiology and Immunology, UCSF, San Francisco, California 94143, USA.

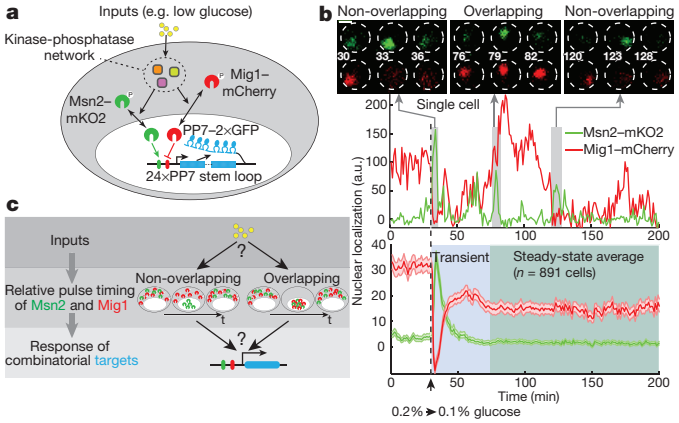

Figure 1 | Temporally structured pulsing of transcription factors Msn2 and Mig1 in response to glucose reduction. **a**, Inputs such as glucose regulate the phosphorylation and nuclear localization of Msn2 and Mig1, which co-regulate some common target genes. Three-colour strains allow simultaneous analysis of Msn2 and Mig1 nuclear localization dynamics and target gene expression. Yeast strains contained Msn2 (green) and Mig1 (red) fluorescent protein fusions, along with a target promoter with (shown) or without (not shown) binding sites for Msn2 and Mig1, driving expression of a transcript containing 24 stem-loops that are specifically bound by the PP7 RNA binding protein fused to 2 × GFP (blue circles). **b**, An example single-cell trace showing nuclear localization dynamics of Msn2 and Mig1. The cell exhibits an immediate temporally structured response to the step in glucose (arrowhead and dashed line), as well as sporadic pulsing throughout the movie. Filmstrips show examples of non-overlapping and overlapping events. White dashed circles indicate cell boundaries and numbers indicate time points. Scale bar is 2 μm. Lower plot shows average trace, revealing the synchronized transient non-overlapping response followed by a constant average response due to unsynchronized pulsing. Shading indicates 95% confidence intervals of the mean (Methods). **c**, These dynamics provoke the questions of how inputs modulate relative timing of Msn2 and Mig1 pulses, and how that timing affects gene regulation.

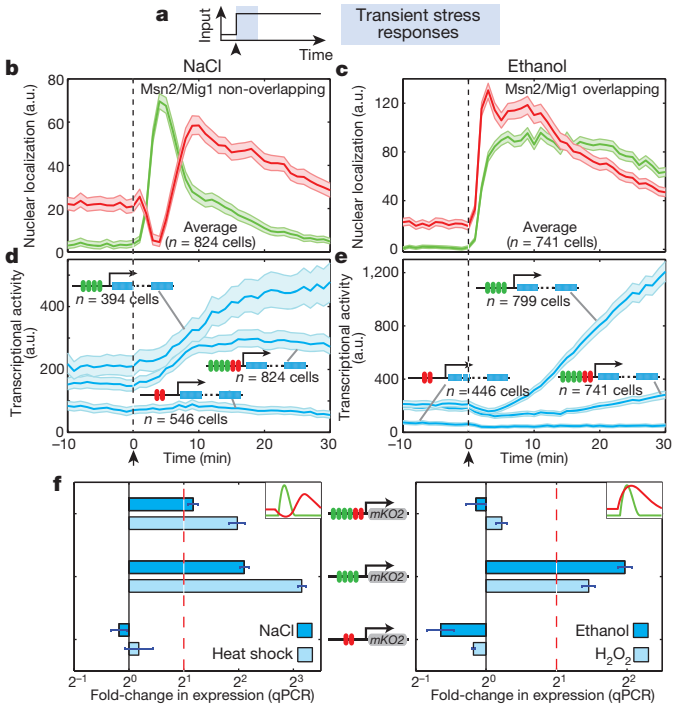

Figure 2 | Different inputs produce distinct transient gene expression responses by modulating relative pulse timing. **a**, Transient nuclear localization and gene expression responses were simultaneously monitored in individual cells. **b**, **c**, Addition of NaCl (100 mM) or ethanol (2.5%) induced non-overlapping and overlapping responses, respectively. Green and red traces show mean Msn2 and Mig1 nuclear localization, respectively. **d**, **e**, Averaged single-cell transcriptional activity traces show that NaCl activated both combinatorial and Msn2-specific targets, while ethanol activated only the Msn2-specific target. Shading in **b**–**e** indicates 95% confidence interval of the mean. **f**, qPCR data are consistent with single-cell data (**b**, **c**), and extend these responses to heat shock and H_2O_2 stresses (Extended Data Fig. 1h, i; see Methods). Error bars indicate s.e.m. calculated from 3–8 biological replicates.

To address these questions, we constructed strains containing synthetic target promoters incorporating binding sites for either or both transcription factors (Fig. 1a). These promoters drove expression of a transcriptional reporter consisting of 24 binding sites for a separately expressed PP7 RNA binding protein fused to green fluorescent protein (GFP)[40] (Fig. 1a). These strains enabled us to simultaneously follow localization dynamics of Msn2 and Mig1 and downstream target expression in the same cell.

Relative pulse timing in the transient response

We first analysed transient responses to changes in various input conditions (that is, different Msn2 stressors) other than the known common input glucose (Fig. 2a). Addition of 100 mM NaCl produced transient non-overlapping pulses of Msn2 and Mig1 in single cells and in population averages (Fig. 2b, Extended Data Fig. 1a–c, Supplementary Video 2) that were similar to those observed in the transient response to glucose reduction (Fig. 1b). Addition of 2.5% ethanol also activated both transcription factors. But in contrast to NaCl, it did so with overlapping, rather than non-overlapping, pulses (Fig. 2c, Extended Data Fig. 1d–f, Supplementary Video 3). The difference in relative timing between NaCl and ethanol was also apparent in cross-correlation analysis (Extended Data Fig. 1g). Together, these results indicate that distinct inputs can generate opposite relative timing in the transient responses of Msn2 and Mig1.

We hypothesized that control of temporal overlap could provide a mechanism for combinatorial gene regulation. Non-overlapping pulse dynamics, in which the activator Msn2 is active, but the repressor Mig1 is not, could activate combinatorial target genes more efficiently than overlapping pulses, in which the two proteins are simultaneously bound to the same target promoter. Indeed, while both NaCl and ethanol led to activation of an Msn2-specific target promoter, only the non-overlapping dynamics of NaCl efficiently induced target expression (Fig. 2d, e, Extended Data Fig. 1a–f). Moreover, we observed similar timing-mediated regulation with other stresses. Heat shock and oxidative stress (from H_2O_2) induced non-overlapping and overlapping dynamics, respectively (Extended Data Fig. 1h, i). As with the other stresses, both non-overlapping and overlapping dynamics activated an Msn2-specific target promoter, but only non-overlapping dynamics efficiently activated the combinatorial target promoter (Fig. 2f). As expected, the dependence of expression from the synthetic combinatorial target promoter on relative timing required both Msn2 and Mig1 (Extended Data Fig. 2a). In addition, these effects were not specific to the synthetic target promoter, as expression of *GSY1* (ref. 41), an endogenous target of Msn2 and Mig1, exhibited similar dependence on relative timing in response to stresses, as shown by both single-cell analysis and quantitative PCR data (Extended Data Fig. 2b–e). In fact, further genome-wide analysis revealed 30 additional endogenous targets that exhibited a similar pattern of gene regulation during transient responses to NaCl and ethanol (Methods, Extended Data Fig. 2f–k, and Supplementary Discussion), suggesting that relative timing-dependent regulation applies to multiple endogenous target genes, as well as to the synthetic promoter. Together these data indicate that, during transient stress responses, cells regulate gene expression by modulating the relative pulse timing between Msn2 and Mig1.

Regulation by relative pulse timing at steady-state

We next asked whether relative pulse timing could also function in constant environmental conditions where both transcription factors

pulse sporadically and repetitively. Because such pulsing is not synchronized among cells, it could only be analysed with single-cell movie data. We observed both overlapping and non-overlapping pulse events under constant conditions (Fig. 1b, Fig. 3a, Extended Data Fig. 3a, b, and Supplementary Videos 4, 5). To better understand the effects of each type of event on gene expression, we adapted the technique of pulse-triggered averaging from neurobiology (usually called spike-triggered averaging)[42] (Extended Data Fig. 3c). We identified Msn2 pulses, and sorted them into two groups depending on whether or not a Mig1 pulse overlapped temporally with the Msn2 pulse (Fig. 3a, Methods). We then averaged the Msn2 and Mig1 dynamics over a time window around the Msn2 pulse peaks, for both overlapping and non-overlapping events. By construction, the resulting pulse-triggered averages showed opposite overall dynamic relationships between the two proteins (Fig. 3b, c).

Pulse-triggered averaging enabled us to analyse the dependence of target gene expression on Msn2 pulsing and, more specifically, on its temporal relationship with Mig1, averaged over variability in both pulsing behaviour and downstream transcriptional responses (see Supplementary Discussion about the multiple layers of variability in this system). Both overlapping and non-overlapping pulses led to subsequent increase in the mean expression of the pure Msn2 synthetic target promoter (Extended Data Fig. 4a–c). However, only the non-overlapping events showed activation of the synthetic combinatorial Msn2-Mig1 promoter or the natural combinatorial target gene, *GSY1* (Fig. 3d, e). Moreover, deletions of the zinc-finger DNA binding domains of either Msn2 or Mig1 eliminated the relative timing-dependence of *GSY1* expression, indicating that DNA-binding of both proteins is necessary for relative timing-dependent regulation (Extended Data Fig. 4d). Together, these results show that relative timing between Msn2 and Mig1 pulses regulates gene expression under steady-state conditions.

Thus far, we have simplified the analysis of relative pulse timing by classifying events as either overlapping or non-overlapping. However, cross-correlation analysis revealed more complexity in the dynamics. For example, we observed a peak at a positive time lag of ~2–4 min, corresponding to sequential activation of Msn2 followed by Mig1 (Extended Data Fig. 4f–i, also evident in Fig. 3c, f; see Supplementary Discussion). More generally, the data showed a continuous distribution of time intervals between a given Msn2 pulse and its previous, or subsequent, Mig1 pulse. To better understand how these dynamics affect target gene expression, we analysed the dependence of mean expression level on the continuous time interval between Msn2 and Mig1 pulses (Extended Data Fig. 5a, b). Mean gene expression is minimal when Msn2 and Mig1 pulse simultaneously, but Mig1 pulses occurring within ~ 4–5 min before or after Msn2 pulses also suppress mean expression. These results are consistent with a model in which Mig1 pulses can both terminate continuing expression from preceding Msn2 pulses, and also establish promoter states with reduced tendency to activate in response to Msn2, possibly due to residual binding of Mig1 itself or to Mig1-induced effects on promoter states. As expected, these extended timing effects required both Msn2 and Mig1 binding sites on the target promoter, as well as DNA-binding activities of both proteins (Extended Data Fig. 5d, e). These characteristic timescales for Msn2-Mig1 pulse interactions establish the degree of simultaneity necessary for pulses to function as overlapping events.

Modulation of relative pulse timing

Having established the effect of relative pulse timing on gene expression at steady-state, we next asked whether and how inputs affect relative timing. We acquired time-lapse movies of Msn2 and Mig1 nuclear localization across a range of constant glucose concentrations (from 0.4% to 0.0125%), where both Msn2 and Mig1 exhibited sporadic nuclear localization pulses (Extended Data Fig. 6, 7b–e). The frequencies of pulses for both proteins, and the mean duration of Mig1 pulses, all varied systematically with glucose concentration (Extended Data Fig. 7a), while mean

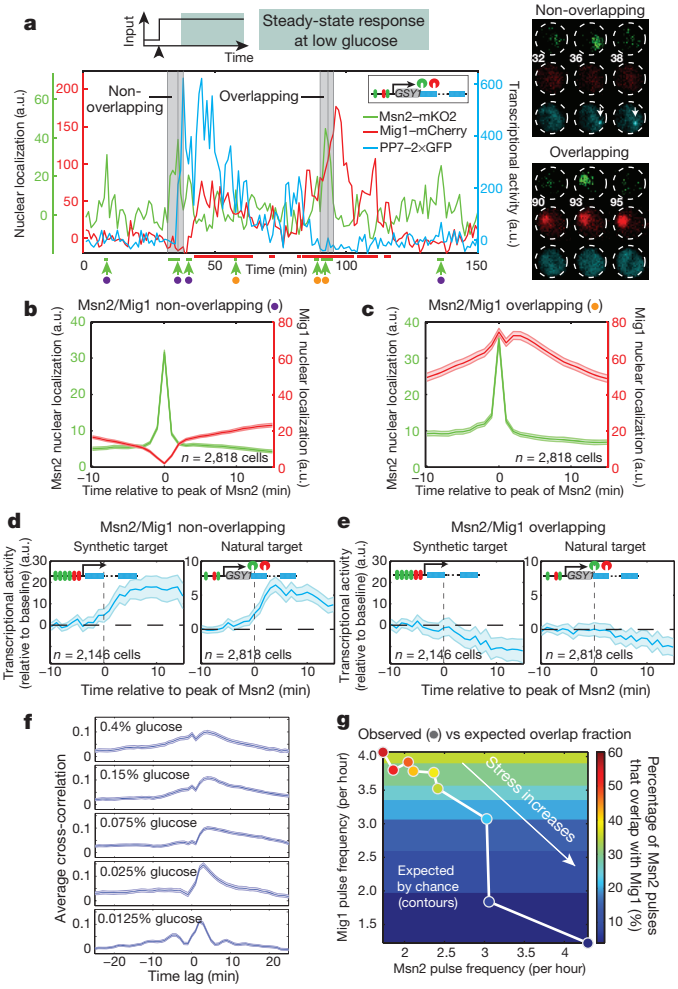

Figure 3 | Pulse-triggered averaging reveals relative pulse timing-dependent gene expression under constant conditions, and modulation of relative timing by glucose concentration. **a**, Localization and target transcription dynamics in a single cell under constant (0.05%) glucose. Msn2 and Mig1 localization are shown in green and red, respectively, while transcriptional activity of their co-regulated target, *GSY1* (*GSY1-24xPP7SL*) is shown in blue. Filmstrips show examples of non-overlapping and overlapping events (indicated by grey shading). White arrows on the upper filmstrip indicate active transcriptional sites for the target gene. Green and red horizontal lines below plot indicate identified Msn2 and Mig1 pulses. Green arrows indicate peaks of the Msn2 pulses used for pulse-triggered averaging (Methods). **b**, **c**, Pulse-triggered averages of Msn2 and Mig1 localization events sorted into non-overlapping (**b**, purple; $n = 14,384$ events) and overlapping (**c**, orange; $n = 7,829$ events) groups. **d**, **e**, Pulse-triggered average transcriptional activity traces for non-overlapping (**d**) and overlapping (**e**) events. Baseline activity (horizontal dashed line) was subtracted from each trace. Traces are aligned to the peak Msn2 pulse at $t = 0$ (vertical dashed line). **f**, Cross-correlation between Msn2 and Mig1 dynamics at different glucose levels (see also Extended Data Fig. 7g). **g**, Glucose levels modulate the percentage of Msn2 pulses that overlap with Mig1. Circles indicate measurements of pulse frequency (location of circle) and the percentage of Msn2 pulses that overlap with Mig1 (overlap fraction, colour of circle) for nine glucose levels (from 0.4% to 0.0125% as in Extended Data Fig. 8a). Horizontal contours indicate the overlap fraction expected at each glucose level assuming independent Msn2 and Mig1 dynamics (Methods). See also controls in Extended Data Fig. 8f, g. Shading indicates 95% confidence intervals of the mean.

pulse amplitudes remained approximately constant (Extended Data Fig. 7a). Interestingly, however, averaged cross-correlations between Msn2 and Mig1 nuclear localization traces showed features (for example, the peak at time lag zero) that depended on glucose concentration (Fig. 3f). Furthermore, the percentage of Msn2 pulses that overlap with Mig1,

which we define as the overlap fraction, changed systematically with glucose concentration (Fig. 3g and Extended Data Fig. 8a). Together, these results indicate that glucose concentration modulates the relative pulse timing between Msn2 and Mig1 at steady-state conditions.

To better understand the effect of glucose concentration on relative pulse timing, it is helpful to distinguish between passive and active types of modulation. Passive modulation arises from changes in the frequency and/or duration of Mig1 pulses, and occurs even if Msn2 and Mig1 dynamics are independent. By contrast, active modulation would require mechanisms that specifically enhance or reduce the fraction of overlapping events.

Passive modulation seems to dominate at lower glucose concentration, but both passive and active modulation occur at higher glucose concentrations. At very low glucose levels (<0.05%), the observed overlap fraction agreed with expectations based on passive modulation only (Methods, lower right of Fig. 3g and Extended Data Fig. 8a). However, at higher glucose levels (≥0.05%), where pulse frequencies became less glucose-dependent (Extended Data Fig. 7a), the observed overlap fraction exceeded the value expected from passive modulation, and increased systematically with glucose concentration (upper left corner of Fig. 3g and Extended Data Fig. 8a), indicating a substantial role for active modulation. Moreover, including the active component of modulation improved the ability of a simple model to explain the dependence of target gene expression on glucose (Extended Data Fig. 8b–d and Supplementary Discussion). We also found that relative pulse timing could be further modulated by other inputs such as NaCl and ethanol (Extended Data Fig. 9 and Supplementary Discussion). These results show that, under steady-state conditions, input identity (type of stress) and level (for example, glucose concentration) together modulate relative pulse timing, through both passive and active mechanisms, to control target gene expression.

Mechanism for relative pulse timing modulation

Relative pulse timing modulation represents a distinct mode of gene regulation that operates in both steady-state and transient conditions (Fig. 4a, see also Supplementary Discussion). What mechanisms could enable cells to actively control relative pulse timing? One possibility involves regulatory components that specifically generate overlapping pulses of Msn2 and Mig1. Previous work has shown that Glc7, the catalytic component of PP1 phosphatase, can indirectly regulate both Msn2 and Mig1 nuclear localization[43], making it a candidate for an active regulator of overlapping pulses (Extended Data Fig. 10a). We constructed a strain in which the wild-type *GLC7* promoter was replaced with a Cu^{2+}-inducible promoter in the native locus. In this strain, reducing expression of *GLC7* below wild-type levels abolished active modulation, making the measured overlap fraction equal to that expected by chance (overlap of red solid and dashed lines in the left panel of Fig. 4b). This effect can also be seen in the Msn2-Mig1 cross-correlation at time lag zero, which is reduced at higher glucose concentrations (compare red and black lines in Fig. 4b, right). Restoring *GLC7* expression close to wild-type levels restored active modulation (blue lines, Fig. 4b). Together, these data (Fig. 4b and Extended Data Fig. 10) support a role for Glc7 in active modulation by glucose (Supplementary Discussion). Other phosphoregulatory components may also contribute to active modulation in these and other conditions.

Discussion

What functions could relative pulse timing modulation provide for the cell? One of the most fundamental concepts in combinatorial regulation is that cooperative interactions between transcription factors can increase their probability of simultaneous binding to a promoter, to implement *cis*-regulatory logic[44]. By controlling the fraction of time that two transcription factors are simultaneously active, relative pulse timing modulation could provide similar effects in *trans*

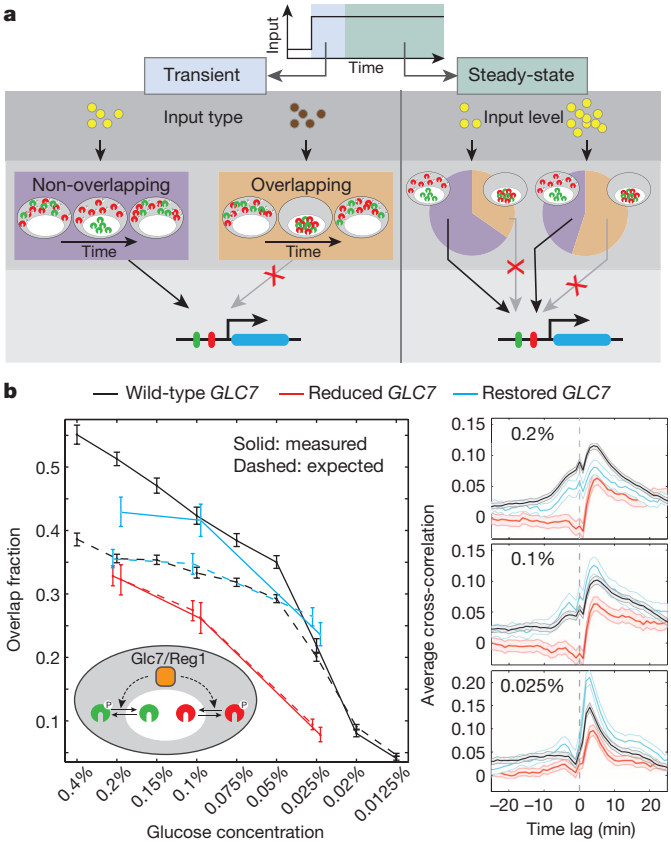

Figure 4 | Mechanistic aspect of relative pulse timing modulation. **a**, In gene regulation by relative pulse timing modulation (schematic), the identity and level of inputs (yellow and brown circles) regulate target gene expression through changes in the relative timing of Msn2 and Mig1 pulses (see Supplementary Discussion). Overlapping events (orange) only activate Msn2-specific targets while non-overlapping events (purple) activate both Msn2-specific and Msn2-Mig1 combinatorial targets. In steady-state (right), inputs modulate the fraction of Msn2 pulses that overlap with Mig1 (pie charts). **b**, *GLC7* mediates active modulation of relative pulse timing, possibly by activating both Msn2 and Mig1 (schematic inset, left). Left, measured (solid line) and expected (dashed line) overlap fractions were plotted for three conditions: wild-type (black), reduced *GLC7* expression (red), and the same strain with *GLC7* expression restored to approximately wild-type levels (blue). Right, average cross-correlation between Msn2 and Mig1 dynamics for three glucose levels (percentages). Shading and error bars indicate 95% confidence intervals of the mean.

(Supplementary Note and Extended Data Fig. 10f–h). In addition to its functionality, a number of basic issues about timing-dependent regulation remain to be understood. For example, what accounts for variability among cells in their transcription factor dynamics and the apparently stochastic response of target promoters to those dynamics? What features of target promoters, such as the kinetic parameters that govern their activation, determine whether and how they respond to timing-based regulation?

Relative timing between signals plays many important roles throughout science and engineering. In neuroscience, the relative timing of action potentials at pre- and post-synaptic neurons controls the strength of synaptic connectivity through spike-timing-dependent plasticity[45]. In communications, modulating the phase of a periodic signal relative to a reference signal is widely used to encode information[46]. Cells seem to have evolved a related strategy by encoding aspects of the extracellular environment in the relative timing with which different transcription factors pulse. The unsynchronized nature of these pulses (at steady-state) has made relative pulse timing modulation rather difficult to detect and characterize previously. However, pulsatile dynamics (both periodic and aperiodic) are now being

discovered in a growing list of central signalling and regulatory pathways[3–5], which are known to interact, or crosstalk, with one another. It will therefore be critical to more systematically map the temporal organization of cellular pathways, and determine principles that can explain both the mechanisms and functions of relative pulse timing modulation in living cells.

Online Content Methods, along with any additional Extended Data display items and Source Data, are available in the online version of the paper; references unique to these sections appear only in the online paper.

Received 2 January; accepted 4 September 2015.
Published online 14 October 2015.

1. Alon, U. *An Introduction to Systems Biology: Design Principles of Biological Circuits*. (Taylor & Francis, 2006).
2. Gertz, J., Siggia, E. D. & Cohen, B. A. Analysis of combinatorial *cis*-regulation in synthetic and genomic promoters. *Nature* **457,** 215–218 (2009).
3. Yosef, N. & Regev, A. Impulse control: temporal dynamics in gene transcription. *Cell* **144,** 886–896 (2011).
4. Purvis, J. E. & Lahav, G. Encoding and decoding cellular information through signaling dynamics. *Cell* **152,** 945–956 (2013).
5. Levine, J. H., Lin, Y. & Elowitz, M. B. Functional roles of pulsing in genetic circuits. *Science* **342,** 1193–1200 (2013).
6. Lahav, G. *et al.* Dynamics of the p53-Mdm2 feedback loop in individual cells. *Nature Genet.* **36,** 147–150 (2004).
7. Nelson, D. E. *et al.* Oscillations in NF-κB signaling control the dynamics of gene expression. *Science* **306,** 704–708 (2004).
8. Cai, L., Dalal, C. K. & Elowitz, M. B. Frequency-modulated nuclear localization bursts coordinate gene regulation. *Nature* **455,** 485–490 (2008).
9. Locke, J. C., Young, J. W., Fontes, M., Hernández Jiménez, M. J. & Elowitz, M. B. Stochastic pulse regulation in bacterial stress response. *Science* **334,** 366–369 (2011).
10. Hao, N. & O'Shea, E. K. Signal-dependent dynamics of transcription factor translocation controls gene expression. *Nature Struct. Mol. Biol.* **19,** 31–39 (2012).
11. Cohen-Saidon, C., Cohen, A. A., Sigal, A., Liron, Y. & Alon, U. Dynamics and variability of ERK2 response to EGF in individual living cells. *Mol. Cell* **36,** 885–893 (2009).
12. Young, J. W., Locke, J. C. & Elowitz, M. B. Rate of environmental change determines stress response specificity. *Proc. Natl Acad. Sci. USA* **110,** 4140–4145 (2013).
13. Levine, J. H., Fontes, M. E., Dworkin, J. & Elowitz, M. B. Pulsed feedback defers cellular differentiation. *PLoS Biol.* **10,** e1001252 (2012).
14. Garmendia-Torres, C., Goldbeter, A. & Jacquet, M. Nucleocytoplasmic oscillations of the yeast transcription factor Msn2: evidence for periodic PKA activation. *Curr. Biol.* **17,** 1044–1049 (2007).
15. Hao, N., Budnik, B. A., Gunawardena, J. & O'Shea, E. K. Tunable signal processing through modular control of transcription factor translocation. *Science* **339,** 460–464 (2013).
16. Hansen, A. S. & O'Shea, E. K. Promoter decoding of transcription factor dynamics involves a trade-off between noise and control of gene expression. *Mol. Syst. Biol.* **9,** 704 (2013).
17. Petrenko, N., Chereji, R. V., McClean, M. N., Morozov, A. V. & Broach, J. R. Noise and interlocking signaling pathways promote distinct transcription factor dynamics in response to different stresses. *Mol. Biol. Cell* **24,** 2045–2057 (2013).
18. Kholodenko, B. N., Hancock, J. F. & Kolch, W. Signalling ballet in space and time. *Nature Rev. Mol. Cell Biol.* **11,** 414–426 (2010).
19. Tay, S. *et al.* Single-cell NF-κB dynamics reveal digital activation and analogue information processing. *Nature* **466,** 267–271 (2010).
20. Batchelor, E., Loewer, A., Mock, C. & Lahav, G. Stimulus-dependent dynamics of p53 in single cells. *Mol. Syst. Biol.* **7,** 488 (2011).
21. Albeck, J. G., Mills, G. B. & Brugge, J. S. Frequency-modulated pulses of ERK activity transmit quantitative proliferation signals. *Mol. Cell* **49,** 249–261 (2013).
22. Yissachar, N. *et al.* Dynamic response diversity of NFAT isoforms in individual living cells. *Mol. Cell* **49,** 322–330 (2013).
23. Kageyama, R., Ohtsuka, T., Shimojo, H. & Imayoshi, I. Dynamic Notch signaling in neural progenitor cells and a revised view of lateral inhibition. *Nature Neurosci.* **11,** 1247–1251 (2008).
24. Martínez-Pastor, M. T. *et al.* The *Saccharomyces cerevisiae* zinc finger proteins Msn2p and Msn4p are required for transcriptional induction through the stress response element (STRE). *EMBO J.* **15,** 2227–2235 (1996).
25. Schmitt, A. P. & McEntee, K. Msn2p, a zinc finger DNA-binding protein, is the transcriptional activator of the multistress response in *Saccharomyces cerevisiae*. *Proc. Natl Acad. Sci. USA* **93,** 5777–5782 (1996).
26. Boy-Marcotte, E., Perrot, M., Bussereau, F., Boucherie, H. & Jacquet, M. Msn2p and Msn4p control a large number of genes induced at the diauxic transition which are repressed by cyclic AMP in *Saccharomyces cerevisiae*. *J. Bacteriol.* **180,** 1044–1052 (1998).
27. Estruch, F. Stress-controlled transcription factors, stress-induced genes and stress tolerance in budding yeast. *FEMS Microbiol. Rev.* **24,** 469–486 (2000).
28. Gasch, A. P. *et al.* Genomic expression programs in the response of yeast cells to environmental changes. *Mol. Biol. Cell* **11,** 4241–4257 (2000).
29. Hasan, R. *et al.* The control of the yeast H_2O_2 response by the Msn2/4 transcription factors. *Mol. Microbiol.* **45,** 233–241 (2002).
30. Morano, K. A., Grant, C. M. & Moye-Rowley, W. S. The response to heat shock and oxidative stress in *Saccharomyces cerevisiae*. *Genetics* **190,** 1157–1195 (2012).
31. Nehlin, J. O., Carlberg, M. & Ronne, H. Control of yeast GAL genes by MIG1 repressor: a transcriptional cascade in the glucose response. *EMBO J.* **10,** 3373–3377 (1991).
32. Lutfiyya, L. L. & Johnston, M. Two zinc-finger-containing repressors are responsible for glucose repression of SUC2 expression. *Mol. Cell. Biol.* **16,** 4790–4797 (1996).
33. Carlson, M. Glucose repression in yeast. *Curr. Opin. Microbiol.* **2,** 202–207 (1999).
34. Teixeira, M. C. *et al.* The YEASTRACT database: an upgraded information system for the analysis of gene and genomic transcription regulation in *Saccharomyces cerevisiae*. *Nucleic Acids Res.* **42,** D161–D166 (2014).
35. Görner, W. *et al.* Nuclear localization of the C2H2 zinc finger protein Msn2p is regulated by stress and protein kinase A activity. *Genes Dev.* **12,** 586–597 (1998).
36. De Vit, M. J., Waddle, J. A. & Johnston, M. Regulated nuclear translocation of the Mig1 glucose repressor. *Mol. Biol. Cell* **8,** 1603–1618 (1997).
37. Treitel, M. A., Kuchin, S. & Carlson, M. Snf1 protein kinase regulates phosphorylation of the Mig1 repressor in *Saccharomyces cerevisiae*. *Mol. Cell. Biol.* **18,** 6273–6280 (1998).
38. Dalal, C. K., Cai, L., Lin, Y., Rahbar, K. & Elowitz, M. B. Pulsatile dynamics in the yeast proteome. *Curr. Biol.* **24,** 2189–2194 (2014).
39. Shaner, N. C., Steinbach, P. A. & Tsien, R. Y. A guide to choosing fluorescent proteins. *Nature Methods* **2,** 905–909 (2005).
40. Larson, D. R., Zenklusen, D., Wu, B., Chao, J. A. & Singer, R. H. Real-time observation of transcription initiation and elongation on an endogenous yeast gene. *Science* **332,** 475–478 (2011).
41. Unnikrishnan, I., Miller, S., Meinke, M. & LaPorte, D. C. Multiple positive and negative elements involved in the regulation of expression of *GSY1* in *Saccharomyces cerevisiae*. *J. Biol. Chem.* **278,** 26450–26457 (2003).
42. Meister, M., Pine, J. & Baylor, D. A. Multi-neuronal signals from the retina: acquisition and analysis. *J. Neurosci. Methods* **51,** 95–106 (1994).
43. De Wever, V., Reiter, W., Ballarini, A., Ammerer, G. & Brocard, C. A dual role for PP1 in shaping the Msn2-dependent transcriptional response to glucose starvation. *EMBO J.* **24,** 4115–4123 (2005).
44. Ptashne, M. *A Genetic Switch: Phage Lambda Revisited* (Cold Spring Harbor Laboratory Press, 2004).
45. Bi, G. Q. & Poo, M. M. Synaptic modifications in cultured hippocampal neurons: dependence on spike timing, synaptic strength, and postsynaptic cell type. *J. Neurosci.* **18,** 10464–10472 (1998).
46. Anderson, J. B., Aulin, T. & Sundberg, C.-E. *Digital Phase Modulation* (Springer, 1986).

Supplementary Information is available in the online version of the paper.

Acknowledgements We thank U. Alon, R. Corral, R. Deshaies, A. Eldar, J. Garcia-Ojalvo, R. Kishony, A. Moses, G. Seelig, P. Swain, and members of the Elowitz laboratory for comments and feedback on the manuscript. We also thank the core sequencing facility at Caltech for help on RNA-Seq. This work was supported by the NIH (R01 GM079771B, R01 GM086793A), the NSF (Award no. 1547056), DARPA (HR0011-05-1-0057), and by the Gordon and Betty Moore Foundation through Grant GBMF2809 to the Caltech Programmable Molecular Technology Initiative. L.C. acknowledges the Ellison foundation for support.

Author Contributions Y.L. and M.B.E. designed experiments. Y.L. performed experiments and analysed data with input from all authors. C.K.D. and L.C. initially observed the correlation between Msn2 and Mig1 dynamics and C.H.S. conducted preliminary analysis of target gene expression. M.B.E. supervised research. Y.L. and M.B.E. wrote the manuscript with input from all authors.

Author Information RNA-Seq data have been deposited at Gene Expression Omnibus (GEO) under the accession code GSE71712. Reprints and permissions information is available at www.nature.com/reprints. The authors declare no competing financial interests. Readers are welcome to comment on the online version of the paper. Correspondence and requests for materials should be addressed to M.B.E. (melowitz@caltech.edu).

METHODS

Strain construction. Standard protocols were used for molecular cloning. Plasmids were replicated in either TOP10 or DH5α *Escherichia coli*. Except where indicated, all yeast strains used in this study were constructed based on BY4741 (*MATa his3Δ0 leu2Δ0 met15Δ0 ura3Δ0*), where *msn4*, *mig2*, *nrg1*, *nrg2* were further deleted (seamless deletion) or compromised (with auxotrophic or drug markers) to avoid complications resulting from these proteins binding to Msn2 or Mig1 binding sites. All yeast transformations were performed with standard lithium-acetate protocol[47] or with Frozen-EZ Yeast Transformation II Kit (Zymo Research). Resulting constructs were confirmed with PCR and/or sequencing. Details of strain genotypes are listed in Supplementary Table 1.

For endogenous gene fusion, *MSN2-mKO2::LEU2* and *MIG1-mCherry::spHIS5* were constructed by the fusion PCR approach where a PCR product comprised of 300–500 bp of 3′ end of target of interest, *mKO2* or *mCherry* gene, *LEU2* or sp*HIS5* cassette, and another 300–500 bp of the target downstream. More specifically, *mCherry*::sp*HIS5* was directly PCR amplified from pKT355 plasmid, *mKO2* gene was obtained from Amalgaam Co., Ltd, and *LEU2* was amplified from pRS315 plasmid. Fused PCR products were directly transformed. For RNA binding protein fusion PP7–2 × GFP, pDZ276 plasmid (a gift from R. Singer) was directly used for transformation into yeast.

Synthetic promoters driving either *24xPP7SL* binding cassette (for single-cell 3-colour movies) or *mKO2* (for qPCR measurements) are composed of the following elements: *ADH1* terminator–UAS–basal *HIS3* promoter (−101 to −1 of *HIS3* gene)–*24xPP7SL* cassette with *ADH1* terminator or *mKO2–KANMAX* or *NATMX* resistance cassette. *ADH1* terminator and *KANMX* cassette were obtained from pKT vectors[48]. *NATMX* was obtained from pAG25 plasmid[49]. Basal *HIS3* promoter was amplified from yeast genome. The *24xPP7SL* cassette was obtained from Addgene (plasmid 31864). mKO2 was used for qPCR analysis because it is exogenous to yeast genome. Three different UAS cassettes contained one or both of the following elements: 4 copies of Msn2 binding motif (GATCTACAGCCCCTGGAAAAT, adopted from *HSP12* promoter[26]) and/or 2 copies of Mig1 binding motif (AATAAAAATGCGGGGAA, adopted from *SUC2* promoter[50]). These UAS cassettes were used to generate Msn2-specific, Mig1-specific, and Msn2-Mig1 combinatorial promoters. The entire constructs were flanked with sequences for integration into *TRP1* locus of BY4741 and were assembled into a pKT based vector. The plasmids were digested with AfeI to release the entire cassette for integration into respective yeast strains. *GSY1-24xPP7SL* (for 3-colour movies) was generated by integration of *24xPP7SL::KANMX* cassette directly downstream of the endogenous *GSY1* gene.

Zinc finger deletion mutants of Msn2 and Mig1 proteins were constructed by direct transformation of PCR fragments containing desired mutations. Specifically, a fused PCR product containing *MIG1(Δamino acid36-91)-mCherry::spHIS5* was used to generate Mig1–mCherry with its DNA binding domain deleted. Similarly, a fused PCR product containing *MSN2(Δaa642-704)-mKO2::LEU2* was used for Msn2 zinc finger mutation. Deletion of Mig1 zinc finger appeared to impact its regulation of nuclear localization as the mutated Mig1–mCherry became much more nuclear localized. This effect, however, does not affect our conclusions.

Copper-inducible *GLC7* strain was constructed by transforming a fusion PCR product of URA3-TEF terminator-*CUP1* promoter flanked with sequences for integration to replace the endogenous *GLC7* promoter. Transformants were selected on plates containing 100 μM $CuSO_4$.

Media and growth conditions. We adopted a minimal media formula with low auto-fluorescence for both culturing yeast cells and for microscopy[8]. Stock solutions for minerals (1,000×), vitamins (1,000×), as well as salts (50×) were made separately. Final working media was made by mixing these three components together with amino acid drop-out mix (from Clontech) and Milli-Q water. Media was adjusted to desired glucose concentration with a glucose stock (40%, w/v).

For overnight liquid culture, single colonies of yeast were picked from agar plates made with minimal media and dispensed into 2–3 ml of minimal media (2% glucose, −Ura or −His −Leu −Ura) in 14 ml round-bottom polypropylene tubes (BD catalogue no. 352059). Cells were grown in a 30 °C shaking incubator. The media and overnight culture procedures were the same for both single-cell microscopy and qPCR experiments. For microscopy, media was supplemented with 2 mM sodium ascorbate (Sigma catalogue no. A7631) and 200 μM trolox (Sigma catalogue no. 238812) (except for media with H_2O_2) to help reduce fluorescent protein photobleaching and photo toxicity to cells.

Time-lapse microscopy. All time-lapse experiments were performed on an Olympus IX81 microscope with 60× objective and hardware autofocus (ZDC2). Fluorescence was excited by a LED light source (Lumencor SOLA Light Engine) and collected onto a scientific CMOS camera (Andor Neo sCMOS) with a 2-by-2 bin setting. For mKO2 and mCherry, single *z*-plane images were acquired. For GFP, a 5-slice *z*-stack was acquired (0.8 μm separation). The excitation and emission filters for mKO2, mCherry and GFP are: Ex 534/20 and Em 572/28, Ex 580/20 and Em 630/60, and Ex 472/30 and Em 535/50, respectively. The frame rate is 1 frame min^{-1}. Time-lapse movie automation was performed with Micro-Manager[51]. The entire microscope room was maintained at ~ 26 °C with two heater fans and a temperature controller (Omega Engineering catalogue no. FCH-FGC20012R and catalogue no. CSC32J).

Movies were acquired for single cells cultured in a dual-inlet microfluidic channel (~500 μm wide), which enables media switching. The microfluidic device was fabricated with polydimethylsiloxane (PDMS) with a Sylgard 184 silicone elastomer kit (DOW Corning) and bonded with 24 mm × 50 mm glass coverslip (Gold Seal No. 1.5) after air-plasma cleaning (Harrick Plasma PDC-32G). The channels were cleaned by brief incubation with 2 M NaOH, followed by washes with 100% ethanol and water. A 15 mg ml^{-1} concanavalin A (Sigma catalogue no. C7275) solution was incubated in the channels for about 10 min to coat the surface for adhering single yeast cells. Channels were washed with media before cell loading. Overnight yeast cultures were diluted back to $OD_{600\ nm} = 0.1$ with 2 ml of fresh media (0.2% glucose, −Ura) and were allowed to grow for another ~3 h. Cells were briefly concentrated by centrifuge and loaded into the channel. Cells were incubated in the channels for 5 min. The device was then loaded onto a sample stage on the microscope. Two inlets of a channel were connected with tubing (Weico Wire&Cable catalogue no. TT-30) to two different media solutions in 10 ml syringes (BD catalogue no. 309604) containing different glucose or stimulant concentrations. These syringes were driven with separate syringe pumps (Harvard Apparatus Pump 11 elite) which were controlled by Micro-Manager. Outlet of the channel was connected to a waste container. Media flow rate was maintained at 5 μl min^{-1} throughout the movie except for during media change (at 50 μl min^{-1} for 2 min).

The starting glucose concentration and the time before media switching differed in different experiments. For the transient glucose shift experiment (Fig. 1b), cells were in the channel with flowing 0.2% glucose media for more than 2 h before switching to 0.1% glucose (acquisition of fluorescent images started 30 min before switching). For experiments in Fig. 2, cells were in the channel with flowing 0.05% glucose media for more than 2 h before switching to 0.05% glucose plus specified stressor. For steady-state experiments in Figs 3, 4, cells were in the channel with flowing 0.2% glucose media for at least 10 min before switching to 0.05% or other designated glucose levels (from 0.4% to 0.0125%). Acquisition of fluorescent images started 110 min after switching media conditions (that is, at steady-state). For cooper inducible *GLC7* experiments (Fig. 4b), cells were cultured with minimal media without the addition of cooper until they were switched to a media containing 10 μM $CuSO_4$ for 110 min before the acquisition of fluorescent images.

Image analysis for extracting single-cell traces. Single-cell traces were extracted from fluorescence images based on cell tracking performed on bright-field images. All analyses were implemented with custom Matlab code (with some modules obtained online as cited below). More specifically, a slightly defocused bright-field image was taken at each frame for segmentation and tracking purposes. Segmentation was performed by circular Hough transformation (CircularHough_Grd function from Mathworks File Exchange). Segmented cell masks were first aligned across the entire movie frames to roughly correct for *x*-*y* stage drift (in order to enhance tracking accuracy). The masks were then fed into a tracking algorithm (u-track[52]) to obtain final cell tracks. Tracks were examined manually, and those with errors were discarded and removed from further analysis. These filtered single-cell tracks were used to extract fluorescence traces.

For analysis of, *z*-stack GFP images (for real-time transcription) we used a maximal intensity z-projection. Fluorescent images were then background subtracted (using background images acquired with media only) and corrected for field flatness caused by uneven illumination (using an image taken with fluorescein). Nuclear localization was calculated by the difference between the mean intensity of the top five pixels and the median intensity of all pixels. Single-cell nuclear localization traces for mKO2 and mCherry were then obtained with tracks obtained above. Real-time transcriptional activity (that is, PP7–2 × GFP signal) was calculated as the intensity of the brightest pixel in the cell minus its local background. For the time when transcription is active, the brightest pixel coincides well with the transcription hotspot. Nuclear localization and transcriptional activity measurements were validated by manual examination of the extracted traces side-by-side with fluorescence images.

Single-cell trace analysis and pulse-triggered averaging analysis. Single-cell traces were first baseline-subtracted and nuclear localization pulses were identified. These pulses were then characterized and used for pulse-triggered averaging analysis. More specifically, calculation of the baselines for mKO2 and mCherry traces was based on a measure for the degree of nuclear localization. In this method, pairwise spatial distance summed over the top 10 brightest pixels in individual cells was used to determine when the fluorescence signal is nuclear

localized or not at a given frame. Nuclear localization scores from frames with the summed distance above a predefined threshold were used to estimate the baseline by a polynomial fit. For cases in which the baseline varied too much along a trace, baseline was estimated by fitting only the nuclear localization values that were below an empirically defined threshold. Baseline for GFP signal was estimated by polynomial fitting the GFP signals that were below an empirically defined threshold. Baseline subtraction procedures were validated by manual examination.

Nuclear localization pulses were identified in both Msn2 and Mig1 traces. Pulse identification was based on iPeak (from Mathworks File Exchange). Shoulder peaks were filtered out and combined with neighbouring peaks (with higher amplitude). The remaining peaks were filtered based on an amplitude threshold (at least 20% above the baseline values) as well as the summed pairwise distance (below a predefined threshold). Width of the pulses was measured for left and right portions of the pulses separately (first fitted with spline and then measured at half of the pulse amplitude or the amplitude threshold, whichever is smaller). For pulse-triggered averaging analysis, a 21 min window around the peak of each Msn2 pulse (that is, 10 min on each side) was used for classifying the relative timing. This time window was chosen based on the frequency of Msn2 pulses. Within this window, all Mig1 pulses were identified. If the peak of a triggered Msn2 pulse fell into the span (defined by pulse width) of a Mig1 pulse, it was classified as an overlapping event. Otherwise, it was classified as a non-overlapping event. A more detailed classification based on the distance between the peak of Msn2 pulse and the edge (defined by pulse width) of the Mig1 pulse (if multiple Mig1 pulses occur within the window, the one with maximum pulse amplitude was chosen for this classification) can also be done as shown in Extended Data Fig. 5. Overlapping and non-overlapping events were averaged separately. Note that a larger time window (that is, a 26 min window with 10 min on the left of the peak and 15 min on the right) was chosen for averaging in Fig. 3 and Extended Data Figs 4, 5 in order to capture and measure the prolonged transcriptional responses in the GFP dynamics.

Cross-correlation analysis. Several figures include cross-correlation analysis (Figs 3f, 4b and Extended Data Figs 1g, 7g and 9d). In these cases, we first compute the cross-correlation function for each cell in a given data set, and then average the resulting functions. Individual cross-correlations were based on mean-subtracted signals and normalized, computed using the following expression:

$$C_{xy}(\tau)=\frac{\langle(x(t)-\langle x\rangle)\cdot(y(t+\tau)-\langle y\rangle)\rangle}{\sqrt{\langle(x(t)-\langle x\rangle)^2\rangle\langle(y(t)-\langle y\rangle)^2\rangle}}$$

Here, angled brackets denote means, and $C_{xy}(\tau)$ is the cross-correlation of $x(t)$ and $y(t)$ at time lag τ.

Quantitative PCR analysis. We used qPCR analysis to validate the single-cell transcriptional response, with similar culture procedures for both microscopy and RNA analysis. In this protocol, cells were exposed to defined stimulants for 10 min and RNA was extracted for two-step RT–qPCR (reverse transcription followed by qPCR). Note that the concentrations of salt, ethanol, and H_2O_2 were doubled when compared to the microfluidic single-cell assay (that is, 200 mM versus 100 mM NaCl, 5% ethanol versus 2.5% ethanol, 0.5 mM versus 0.25 mM H_2O_2). Overnight cultures were diluted to $OD_{600\,nm}=0.075$ with 20 ml of 0.2% glucose (−Ura) in 250 ml flask and allowed to grow until the $OD_{600\,nm}$ reached above 0.2 (about 3–4 h). For transient stress experiments, cultures were then diluted back to $OD_{600\,nm}=0.2$ with 20 ml of 0.05% glucose in 250 ml flask and allowed to grow for another 2 h. Cultures were split into 14 ml polypropylene tubes (4 ml each). Stresses were applied by mixing concentrated stock solutions (such as 5 M NaCl, 100% ethanol, 0.83 M H_2O_2) with the culture or by moving the culture tubes to a 37 °C shaking incubator (for heat shock). After precisely 10 min of stress application, each culture was mixed with 6 ml pre-chilled methanol (with dry ice/ethanol bath) in a 50 ml tube to rapidly fix the cells. For steady-state experiments, cells were diluted to $OD_{600\,nm}=0.1$ with 4 ml fresh media of designated condition (different glucose concentration with or without additional $CuSO_4$) in 50 ml falcon tube. Cultures were allowed to grow for 2 h and cells were mixed quickly with cold methanol as above. After >1 h in cold methanol, cells were collected by centrifuging at 4 °C and washed with ice cold water. Prior to performing standard RNA extraction protocols (with on-column DNase digestion) with RNeasy mini kits (Qiagen), cells were enzymatically treated with 100 µl of 2 U μl^{-1} lyticase solution (Sigma catalogue no. L2524) for 10 min at 30 °C. The extracted RNA absorbance spectrum was analysed with NanoDrop and 1 µg RNA was used for a standard 20 µl iScript (Bio-Rad) reverse transcription reaction. The resulting cDNA was diluted 4× with water before proceeding to qPCR reaction. A typical 10 µl qPCR reaction was assembled with 5 µl iQ SYBR Green Supermix (Bio-Rad), 2 µl primers (1.5 µM each), 2 µl of cDNA, and 1 µl of water. Reactions were performed on a CFX96 Real-Time machine (Bio-Rad). Each reaction had ≥2 technical replicates. Three reference genes were included (*ACT1, UBC6, TFC1*) for each sample. The latter two were based on recommendations by Teste *et al.*[53]. The mean *C*q values of these reference genes were used for the calculation of ΔΔ*C*q (or fold-change as $2^{-\Delta\Delta Cq}$) for each gene between sample and control. Calculations of ΔΔ*C*q were done by CFX Manager Software (Bio-Rad) and final processing was performed by Matlab (Mathworks). Error bars were calculated by taking the standard errors of ≥3 biological replicates. Primers were designed according to manufacture instructions for iQ SYBR Green and were blasted against the yeast transcriptome (Primer-Blast[54]) to avoid nonspecific priming. The following primer sequences were used:

ACT1_F: ACATCGTTATGTCCGGTGGT; ACT1_R: CATGGAAGATGGAGCCAAAG; UBC6_F: AGGACCTGCGGATACTCCTT; UBC6_R: TCTGATAGCCGGTGGTTTGT; TFC1_F: AGCGCTGGCACTCATATCTT; TFC1_R: TTGGGCGTATTCCACTGAAC; mKO2_F: GTGATCAAGCCCGAGATGAA; mKO2_R: CATCTCCTGATGTCCCTCGT; GSY1_F: ACTGGTTGATTGAGGGAGCA; GSY1_R: GACCATAGGTCAGCCTTCCA; EMI2_F: AATGGTGACGGAACCTTTGA; EMI2_R: GCGACCCAGGTAGCTAAACA; GLC3_F: CCGCTCCATAGGTGGTACTG; GLC3_R: ACTTCCCATCTCCCATTCATC; GPH1_F: TCTGGCCACCCATGAATTAG; GPH1_R: GCAACGCTCAGGACACTCTT; IGD1_F: AGCAATGGTAACAGCGCAAG; IGD1_R: CTCCAAACATGTGAAGCTGGT.

RNA-Seq library construction and data analysis. For data shown in Extended Data Fig. 2, RNA-Seq was performed with libraries prepared from the RNA samples collected from cells of three different strains (no deletion strain and deletions of either *msn2* or *mig1*) subjected to no treatment (control), 200 mM NaCl, or 2.5% ethanol. For data shown in Extended Data Fig. 8d, RNA-Seq was performed with libraries prepared from the RNA samples collected from cells of the no deletion strain across 9 glucose concentrations and one *msn2* deletion strain at 0.2% glucose. RNA sample preparation was similar to the descriptions in the previous section. Library was constructed according to standard Illumina protocols. Sequencing was performed on a HiSeq 2500 sequencer. Both library construction and sequencing were performed at the core sequencing facility at Caltech. For the transient experiments, two biological replicates for each sample collected on different days were sequenced and analysed. Analysis of the sequencing data was performed with a local instance of Galaxy[55]. A standard analysis pipeline was used (alignment with Tophat[56]). Statistical test of differential expression between conditions was performed with duplicates using DESeq2[57].

Calculation of expected-by-chance fraction of overlapping pulsing. The heat map in Fig. 3g showed the expected fraction of Msn2 pulses that overlap with Mig1 pulses. This expected fraction measures the percentage of Msn2 pulses that would coincide with Mig1 pulses assuming the factors pulse independently of each other. Because an overlapping event is defined as when the peak of an Msn2 pulse falls into the time span of a Mig1 pulse, its expected fraction can be calculated as the fraction of time that Mig1 pulses occupy and is independent of Msn2 frequency, that is, $\frac{\text{number of Mig1 pulses per hour}\times\text{mean Mig1 duration}}{1\text{ hour}}$. As shown in Extended Data Fig. 8a, this calculated expected-by-chance overlap fraction is almost identical to the measured overlap fraction from an artificial population of cells where Msn2 and Mig1 dynamics are scrambled to enforce independence.

Fitting gene expression data with different models. In Extended Data Fig. 8b–d, we compared the ability of three models to fit combinatorial target gene expression levels across a range of glucose concentrations. The first model ('active–passive') includes both active and passive modulation, the second model ('passive only') includes only passive modulation, that is, assumes independent Msn2 and Mig1 dynamics, and the third model ('Msn2 only') assumes Mig1 does not reduce the effect of the Msn2 pulses (see Supplementary Discussion). In all models, gene expression is assumed to be activated by Msn2 and also occur at a basal level in the absence of nuclear Msn2. Mig1 is assumed to suppress both Msn2-activated (except in the Msn2 only model), and basal expression. In these models, expression is thus proportional to the frequency of effective Msn2 pulses (those not suppressed by Mig1 pulses, see definition below), plus the promoter-specific basal activity:

$$E^i_{\text{model}}=a\cdot f^i_{\text{Msn2eff}}+b\cdot\theta^i_{\text{Mig1out}}$$

Here, i labels the glucose condition; a denotes the mean amount of gene expression produced by each effective Msn2 pulse; f^i_{Msn2eff} is the frequency of effective Msn2 pulses per hour (calculated based on single-cell data, see details below); b is the basal promoter activity when Mig1 is out of the nucleus; and $\theta^i_{\text{Mig1out}}$ is the fraction of time that Mig1 is out of the nucleus (also calculated based on single-cell data). Note that the three models differ only in the effective Msn2 pulse frequency. In general, the active-passive model has the lowest f^i_{Msn2eff}, because

in this model Mig1 pulses suppress the effects of Msn2 pulses even more frequently than expected if Msn2 and Mig1 were independent, that is, in the 'passive only' model. In contrast, the 'Msn2 only' model has the highest f^i_{Msn2eff}.

We calculated the effective Msn2 frequency, f^i_{Msn2eff}, with two different levels of temporal precision (see Supplementary Discussion). The simpler binary relative timing model considers Msn2 pulses to be either overlapping or non-overlapping with Mig1, as in Fig. 3. By contrast, the more precise continuous relative timing model allows for the empirically observed continuous dependence of expression level on the time interval between the Msn2 and Mig1 pulses, as shown in Extended Data Fig. 5b.

In the binary model, the effective Msn2 pulse frequency is simply the frequency of non-overlapping Msn2 pulses (Fig. 3). In the continuous model, the effect of an observed Msn2 pulse on a natural target's gene expression was determined by its pulse timing relative to Mig1 using the results in Extended Data Fig. 5b. More specifically, we normalized the data in Extended Data Fig. 5b such that Msn2 only pulses (those at the longest absolute time intervals) have a relative expression level of 1, while overlapping Msn2 pulses (time interval 0) have a relative expression level of 0. For each observed Msn2 pulse we calculated an effective gene expression contribution based on its timing relative to Mig1. This calculation was performed across all traces and all glucose concentrations to obtain f^i_{Msn2eff}. Prior to fitting, we converted the relative qPCR expression data to an absolute scale (equivalent to FPKM, fragments per kilobase of transcript per million mapped reads) using the RNA-seq data at 0.05% glucose as a reference (Extended Data Fig. 2f). We also used RNA-seq data from an *msn2* mutant to independently estimate parameter *b*. Thus, for each of the three models, only the parameter *a* needs to be fit. The least-squares fitting was performed by minimizing the error function $\sum_{i=1}^{9}\left[E^i_{\mathrm{model}}-E^i_{\mathrm{exp}}\right]^2$, where E^i_{exp} denotes the experimentally measured gene expression levels at glucose level *i* from qPCR and RNA-seq data sets.

Statistical analysis. To compare single-cell data between different conditions, we computed the 95% confidence intervals of the sample mean for each set of single cells by the bootstrap method. More specifically, resampling with replacement was implemented with Matlab and 2,000 resamplings of the same sample size were obtained for each set of single cells. These 2,000 sets of single-cell data were then used for downstream analysis such as pulse-triggered averaging analysis and others. Bias-corrected 95% confidence interval[58] of the 2,000 samples were then calculated and represented as error bars or shaded regions. To compare distributions, the Kolmogorov–Smirnov test was used.

No statistical methods were used to predetermine sample size. The experiments were not randomized, and the investigators were not blinded to allocation during experiments and outcome assessment.

47. Gietz, R. D. & Schiestl, R. H. High-efficiency yeast transformation using the LiAc/SS carrier DNA/PEG method. *Nature Protocols* **2,** 31–34 (2007).
48. Sheff, M. A. & Thorn, K. S. Optimized cassettes for fluorescent protein tagging in *Saccharomyces cerevisiae*. *Yeast* **21,** 661–670 (2004).
49. Goldstein, A. L. & McCusker, J. H. Three new dominant drug resistance cassettes for gene disruption in *Saccharomyces cerevisiae*. *Yeast* **15,** 1541–1553 (1999).
50. Lutfiyya, L. L. *et al.* Characterization of three related glucose repressors and genes they regulate in *Saccharomyces cerevisiae*. *Genetics* **150,** 1377–1391 (1998).
51. Edelstein, A., Amodaj, N., Hoover, K., Vale, R. & Stuurman, N. Computer control of microscopes using μManager. *Curr. Protoc. Mol. Biol.* Unit 14.20 (2010).
52. Jaqaman, K. *et al.* Robust single-particle tracking in live-cell time-lapse sequences. *Nature Methods* **5,** 695–702 (2008).
53. Teste, M. A., Duquenne, M., François, J. M. & Parrou, J. L. Validation of reference genes for quantitative expression analysis by real-time RT-PCR in *Saccharomyces cerevisiae*. *BMC Mol. Biol.* **10,** 99 (2009).
54. Ye, J. *et al.* Primer-BLAST: a tool to design target-specific primers for polymerase chain reaction. *BMC Bioinformatics* **13,** 134 (2012).
55. Goecks, J., Nekrutenko, A., Taylor, J., The Galaxy Team. Galaxy: a comprehensive approach for supporting accessible, reproducible, and transparent computational research in the life sciences. *Genome Biol.* **11,** R86 (2010).
56. Trapnell, C. *et al.* Differential gene and transcript expression analysis of RNA-seq experiments with TopHat and Cufflinks. *Nature Protocols* **7,** 562–578 (2012).
57. Love, M. I., Huber, W. & Anders, S. Moderated estimation of fold change and dispersion for RNA-seq data with DESeq2. *Genome Biol.* **15,** 550 (2014).
58. Efron, B. *The Jackknife, the Bootstrap, and Other Resampling Plans* (Society for Industrial and Applied Mathematics, 1982).

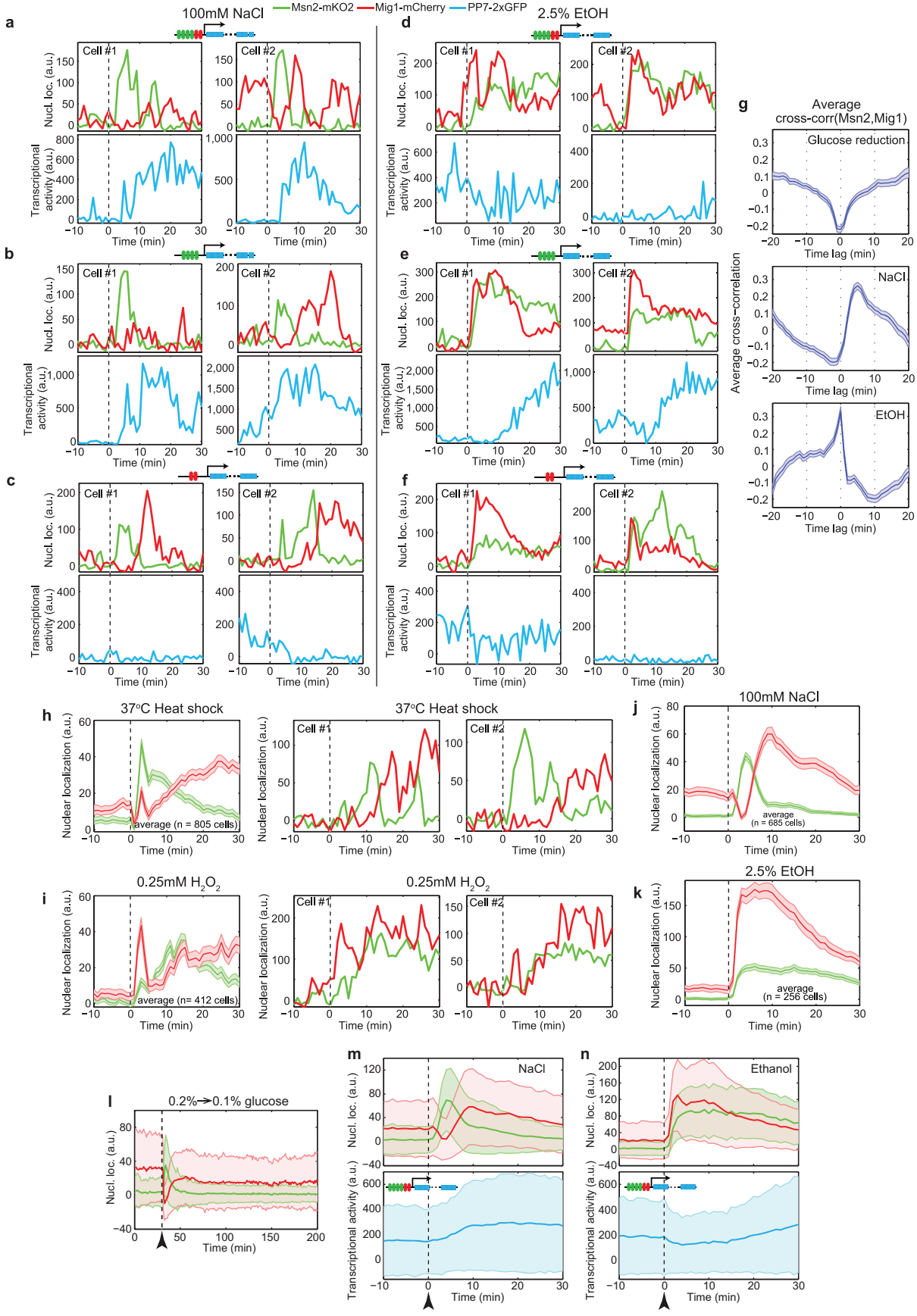

Extended Data Figure 1 | Single-cell analysis of relative pulse timing modulation by stress identity during transient response. **a**–**c**, Example traces for synthetic combinatorial (**a**), Msn2-specific (**b**), or Mig1-specific (**c**) promoters, in response to addition of 100 mM NaCl. Two cells are shown for each strain. For each cell, Msn2 and Mig1 localization traces (green and red) and the corresponding promoter response (blue) are shown on separate panels (top and bottom). Vertical dashed line indicates time of NaCl addition. **d**–**f**, Similar example traces for the response to addition of 2.5% ethanol. **g**, Average cross-correlation function of the transient Msn2 and Mig1 responses from $t = 0$–30 min after indicated stress. Cross-correlation between Msn2 and Mig1 is negative at time lag zero for both glucose reduction and NaCl stresses, but positive for ethanol stress. **h**, **i**, Averaged (left) and single-cell (right) nuclear localization traces of Msn2–mKO2 and Mig1–mCherry in response to 37 °C heat shock (**h**) or 0.25 mM H_2O_2 (**i**). **j**, **k**, Msn2 and Mig1 dynamics observed in Fig. 2b, c do not depend on the deletions introduced to the strain background. Averaged nuclear localization traces of Msn2–mKO2 and Mig1–mCherry in response to 100 mM NaCl (**j**) or 2.5% ethanol (**k**) for a control strain without *msn4 mig2* deletions. Shading indicates 95% confidence intervals of the mean. **l**–**n**, Standard deviation representations of different sets of single-cell data (presented in main figures). The mean is indicated with a solid line, and ± 1 standard deviation ranges are indicated by shading. **l**, Nuclear localization responses of Msn2–mKO2 (green) and Mig1–mCherry (red) to downshift in glucose level (see Fig. 1b). **m**, **n**, Nuclear localizations and transcriptional responses to NaCl and ethanol. (see Fig. 2b, c).

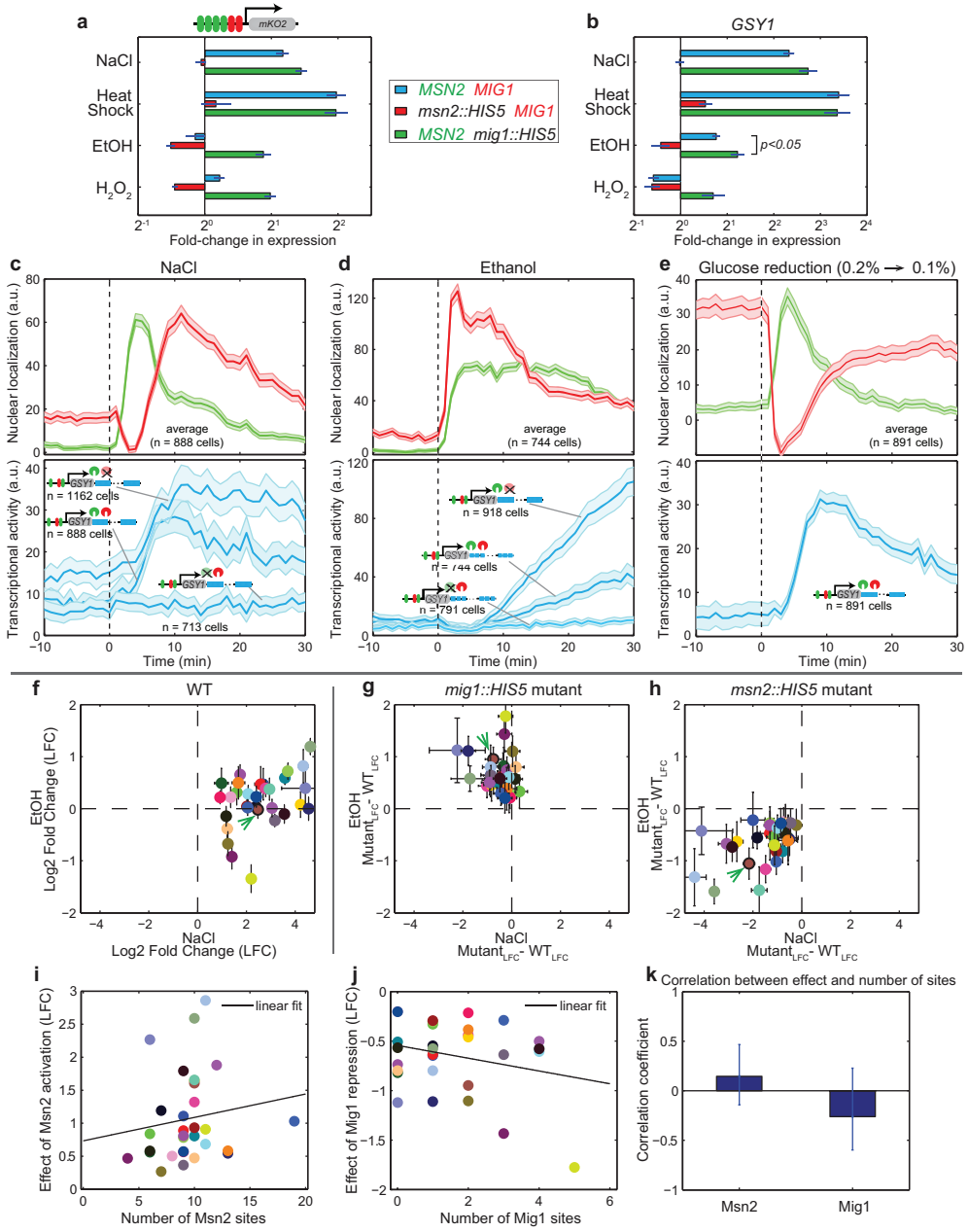

Extended Data Figure 2 | Additional data and analysis for transient stress responses. **a**, Fold-change in expression in response to different stresses for synthetic combinatorial target gene for three genetic backgrounds: no deletion (*MSN2 MIG1*, data from Fig. 2f), *msn2* deletion, and *mig1* deletion. **b**, Similar plot for the endogenous target gene *GSY1*. Cells were treated with designated stress for 10 min and ≥ 3 biological replicates were averaged (error bar indicates s.e.m.). *P* value was obtained from two-tailed *t*-test. **c**, **d**, Averaged transcriptional responses of *GSY1-24xPP7* in response to 100 mM NaCl (**c**) or 2.5% ethanol (**d**) for three genetic backgrounds: no deletion, *mig1* deletion, and *msn2* deletion. Averaged nuclear localization traces of Msn2–mKO2 and Mig1–mCherry for the 'no deletion' strain are shown on the top panels. **e**, Averaged nuclear localization traces of Msn2–mKO2 and Mig1–mCherry (top) and corresponding transcriptional responses for *GSY1-24xPP7* in response to glucose downshift (from 0.2% to 0.1%). Shading in **c**–**e** indicates 95% confidence intervals of the mean. **f**–**k**, RNA-seq analysis (see Methods and Supplementary Discussion for more details). **f**, $\log_2$ fold-changes (LFC) in gene expression of 31 identified combinatorial targets (including *GSY1*; brown circle, indicated by green arrow) in response to NaCl (*x* axis) and ethanol (*y* axis) for wild-type background (that is, no deletion of either *MSN2* or *MIG1*). **g**, The differences in LFC between wild-type and *mig1* deletion for both NaCl (*x* axis) and ethanol (*y* axis). **h**, The differences in LFC between wild-type and *msn2* deletion for both NaCl (*x* axis) and ethanol (*y* axis). **i**, The effect of Msn2 for each target was plotted against the corresponding number of Msn2 binding sites. **j**, Analogous plot for the effect of Mig1 binding sites. **k**, Correlation coefficients between the effect of Msn2 or Mig1 and the number of Msn2 or Mig1 binding motif, respectively. Error bars in **f**–**h** indicate standard deviations from two biological replicates. Error bars in **k** represent 95% confidence intervals from bootstrap.

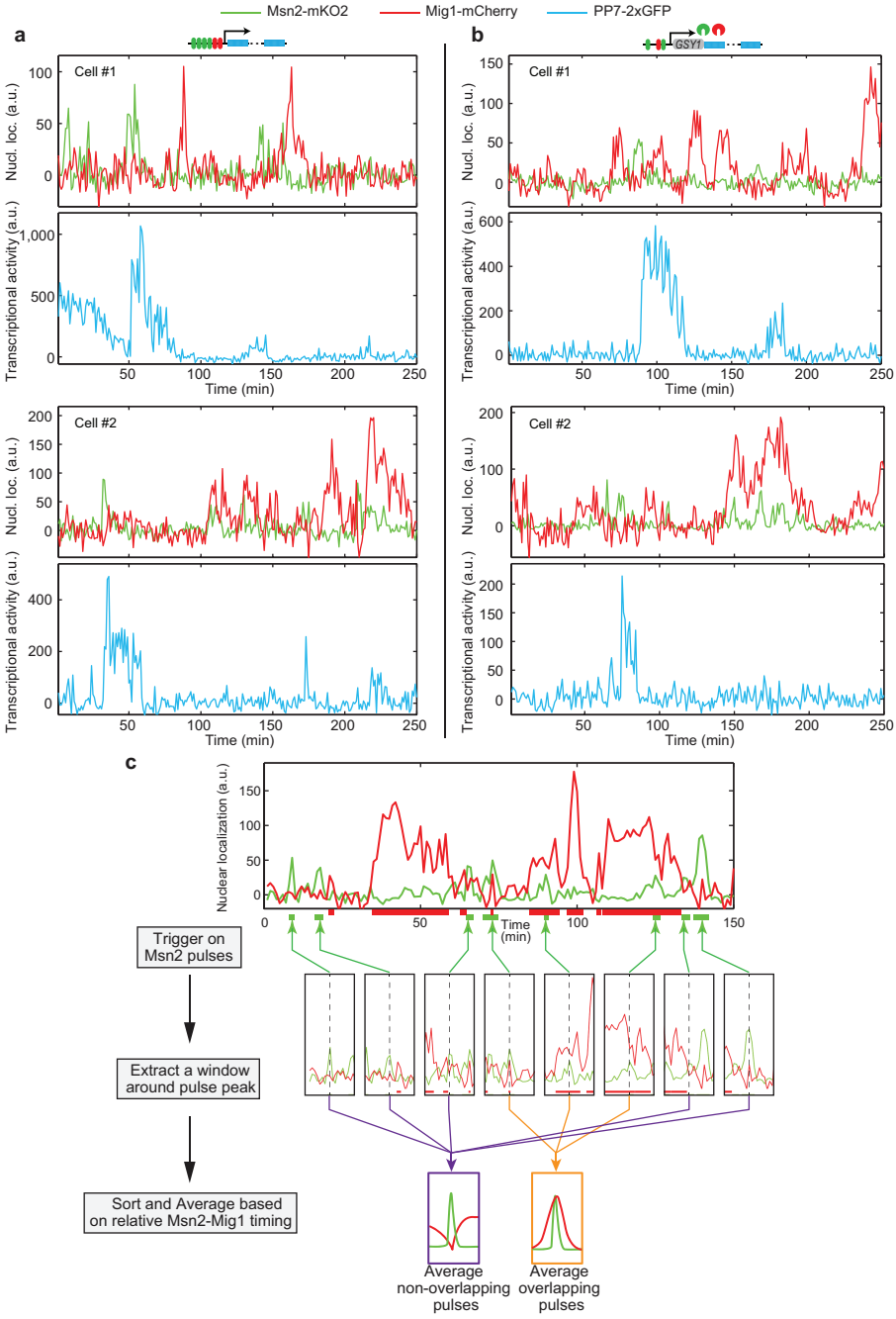

Extended Data Figure 3 | Example 3-colour single-cell traces under steady-state conditions, and schematic diagram of pulse-triggered averaging analysis. **a**, **b**, Example 3-colour single-cell traces for synthetic (**a**) and natural (**b**) promoters under constant glucose (0.05%). Two cells are shown for each promoter. For each cell, nuclear localization traces are shown on the top and PP7–2 × GFP transcriptional output signal is shown on the bottom. **c**, Schematic illustration of pulse-triggered averaging analysis. Msn2 pulses were identified (green arrows) and sorted based on their relationship with the Mig1 signal within a 21 min time window (see Methods). Horizontal green and red lines underneath top time trace plot indicate width of identified Msn2 and Mig1 pulses, respectively. Msn2 pulses whose peaks overlap with Mig1 pulses were categorized as overlapping events (orange arrows) while the rest of Msn2 pulses were categorized as non-overlapping events (purple arrows). Overlapping and non-overlapping events were then averaged separately (bottom schematics).

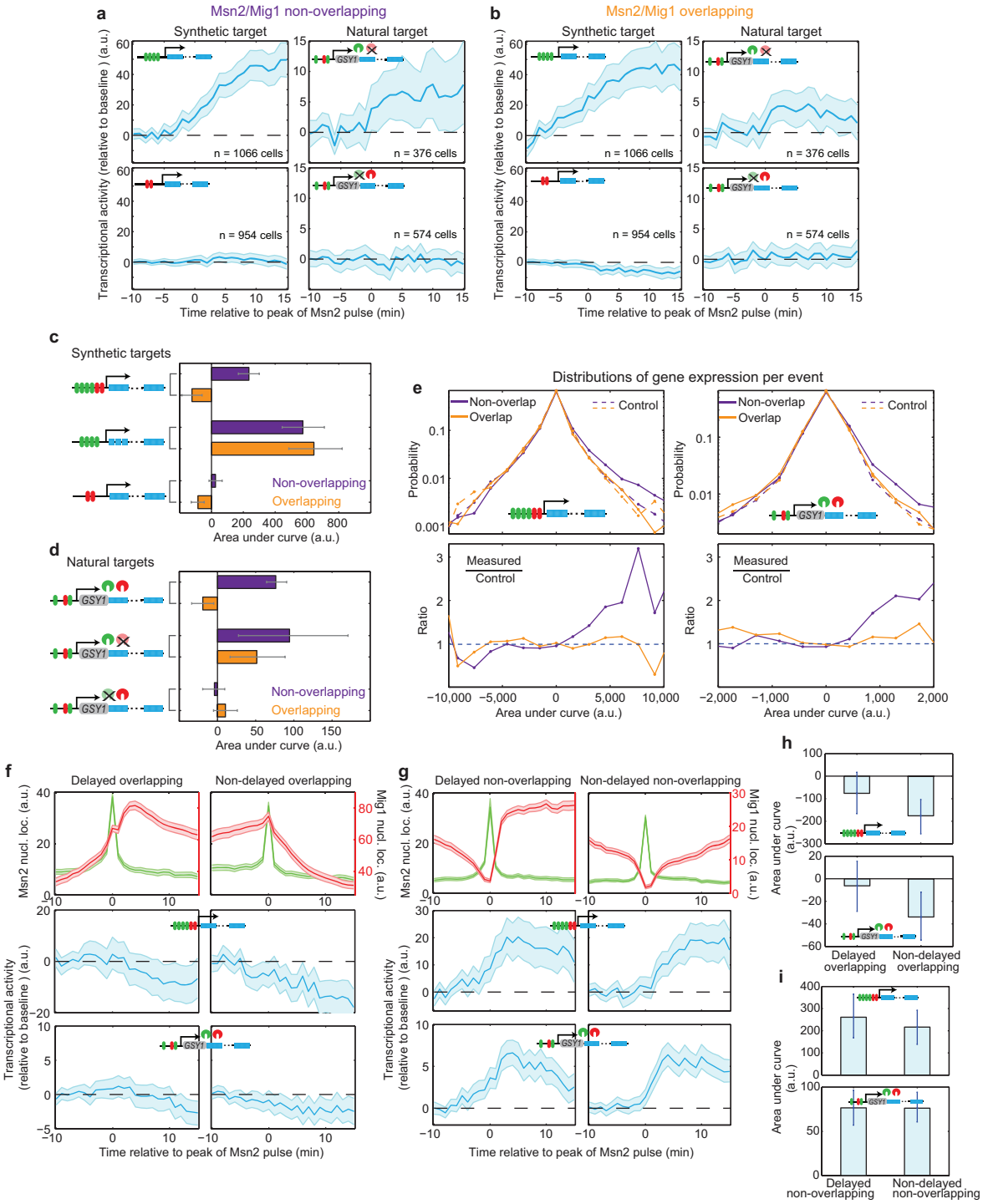

Extended Data Figure 4 | Pulse-triggered averaging analysis for control promoters and for delayed pulse timing events. **a**, **b**, Plots analogous to those in Fig. 3d, e for additional synthetic and natural promoters. The *GSY1* promoter was examined in strains with Msn2 or Mig1 zinc-finger deletions. For gene expression, areas under curves were analysed and presented in **c**, **d**. **c**, Relative pulse timing-dependent gene expression occurs for combinatorial promoters but not pure Msn2 or Mig1 target promoters. Bars represent integrated gene expression based on area under curve from Fig. 3d, e and **a**, **b**. **d**, Plot analogous to **c** for the natural *GSY1* target gene. Binding of the transcription factors was abolished by mutations in zinc finger DNA-binding domains, indicated by crosses. **e**, Distributions of gene expression (estimated as integrated area under curve) per non-overlapping or overlapping event for both synthetic and natural combinatorial promoters (real data (solid) versus control data (dashed); top) and ratios between real and control data (bottom). Control data was measured from scrambled population of cells. For the real data, the distributions of non-overlapping and overlapping events are significantly different (by Kolmogorov–Smirnov test) with P values of 2.1×10^{-17} and 1.2×10^{-15} for synthetic and natural promoters, respectively. In contrast, for control data, they are not significantly different (P values: 0.4520 and 0.9888). For the calculation of ratios, averages of the non-overlapping and overlapping control data were used as control. **f**–**i**, Pulse-triggered averaging analysis of 'delayed' events in which an Msn2 pulse is followed by a Mig1 pulse (see Supplementary Discussion for details). **f**, Overlapping events were subdivided into delayed and non-delayed depending, as shown. Corresponding mean Msn2 and Mig1 signals as well as transcriptional responses were plotted for both synthetic and natural promoters. A similar classification was performed for non-overlapping events (**g**). Area under curve for **f**, **g** was plotted for direct comparison of gene expression between delayed and non-delayed pulse timing events (**h**, **i**). Shading and error bars indicate 95% confidence intervals of the mean. Schematic promoters indicate whether the synthetic or natural *GSY1* promoter were used in each case.

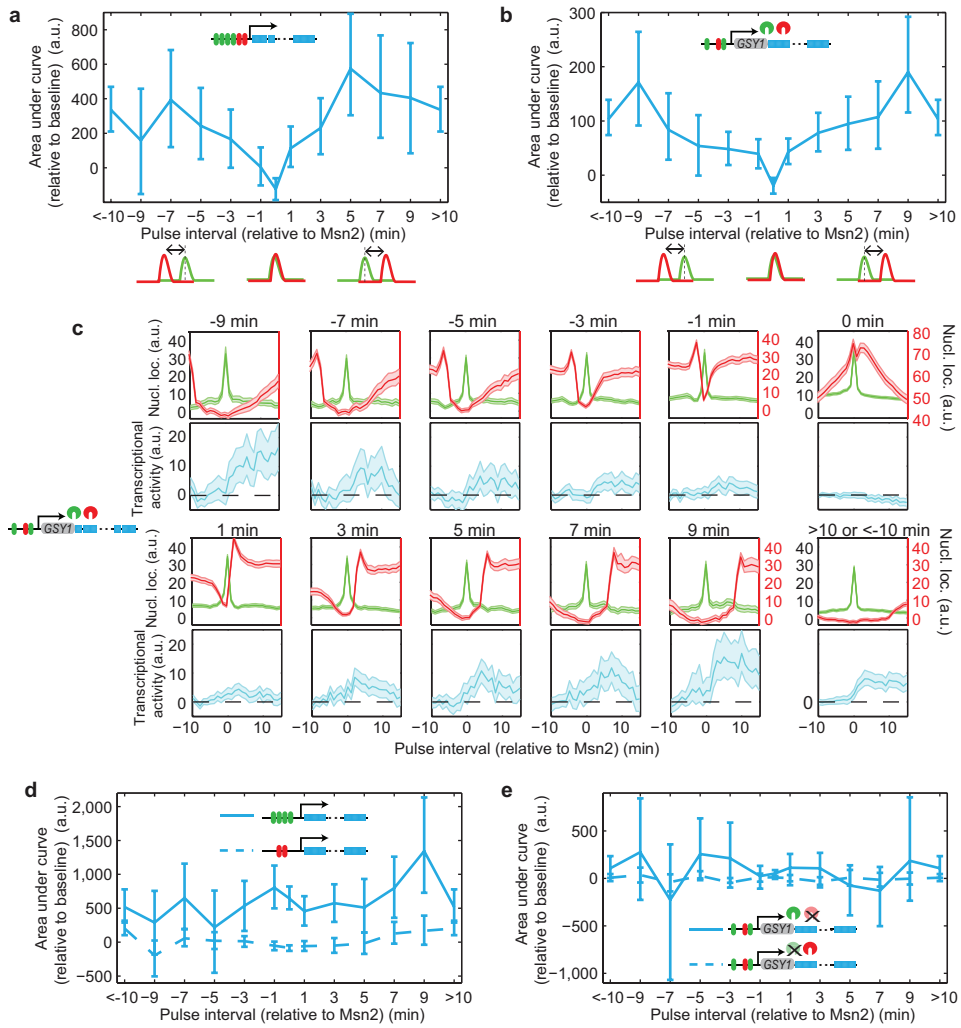

Extended Data Figure 5 | Analysis of mean gene expression dependence on time interval (continuous relative timing) between Msn2 and Mig1 pulses. **a**, **b**, Mean expression from both synthetic (**a**) and natural (**b**) target promoters depends on the time interval between Msn2 and Mig1 pulses (that is, interval between the peak of an Msn2 pulse and the edge of the nearest Mig1 pulse). For each time interval, mean expression values were determined by integrating the area under the baseline-subtracted averaged PP7 traces, and averaging within bins of similar pulse interval. **c**, Specifically, Msn2 pulses were categorized on the basis of the pulse interval between Msn2 and Mig1 and the corresponding PP7 signals were averaged and their areas under curve were plotted (Methods). The pulse interval ranges from −9 to 9 min, which represents the bin centre of each 2-min bin (for example, 1 min represents the range 2 min ≥ interval > 0 min), with the 0 min interval representing overlapping events. Both >10 or <−10 min intervals represent events where Msn2 pulses were not surrounded by any Mig1 pulses within 21 min. **d**, **e**, Msn2 and Mig1 regulation are both necessary for continuous relative timing-dependent gene expression under constant glucose condition. Analysis similar to **a**, **b** was performed on synthetic Msn2- and Mig1-specific promoters (**d**) and natural *GSY1* promoter with Msn2 or Mig1 zinc finger deletion mutants (**e**). Shading and error bars indicate 95% confidence intervals of the mean.

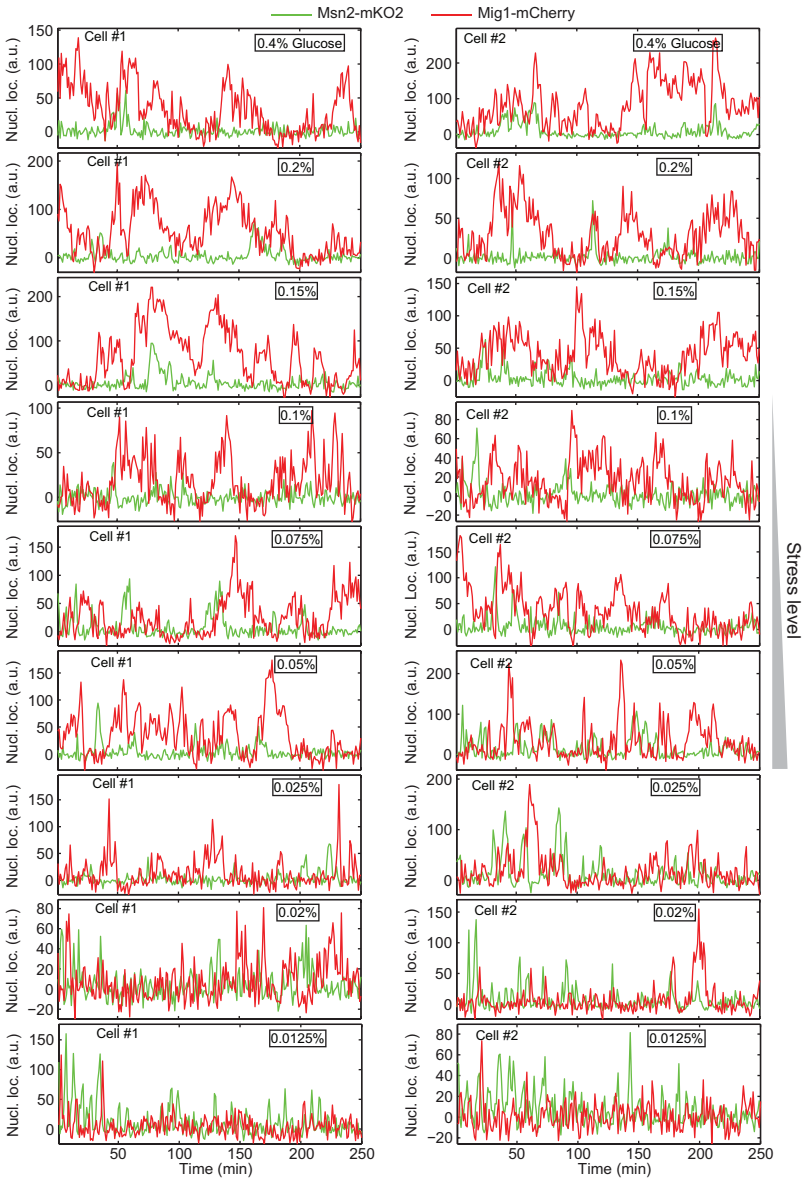

Extended Data Figure 6 | Example single-cell nuclear localization traces for different constant glucose conditions. Two single-cell traces are shown for each indicated glucose level (boxed percentage values). Cells were switched to indicated glucose level from 0.2% glucose at 110 min before time zero (that is, beginning of movie acquisition).

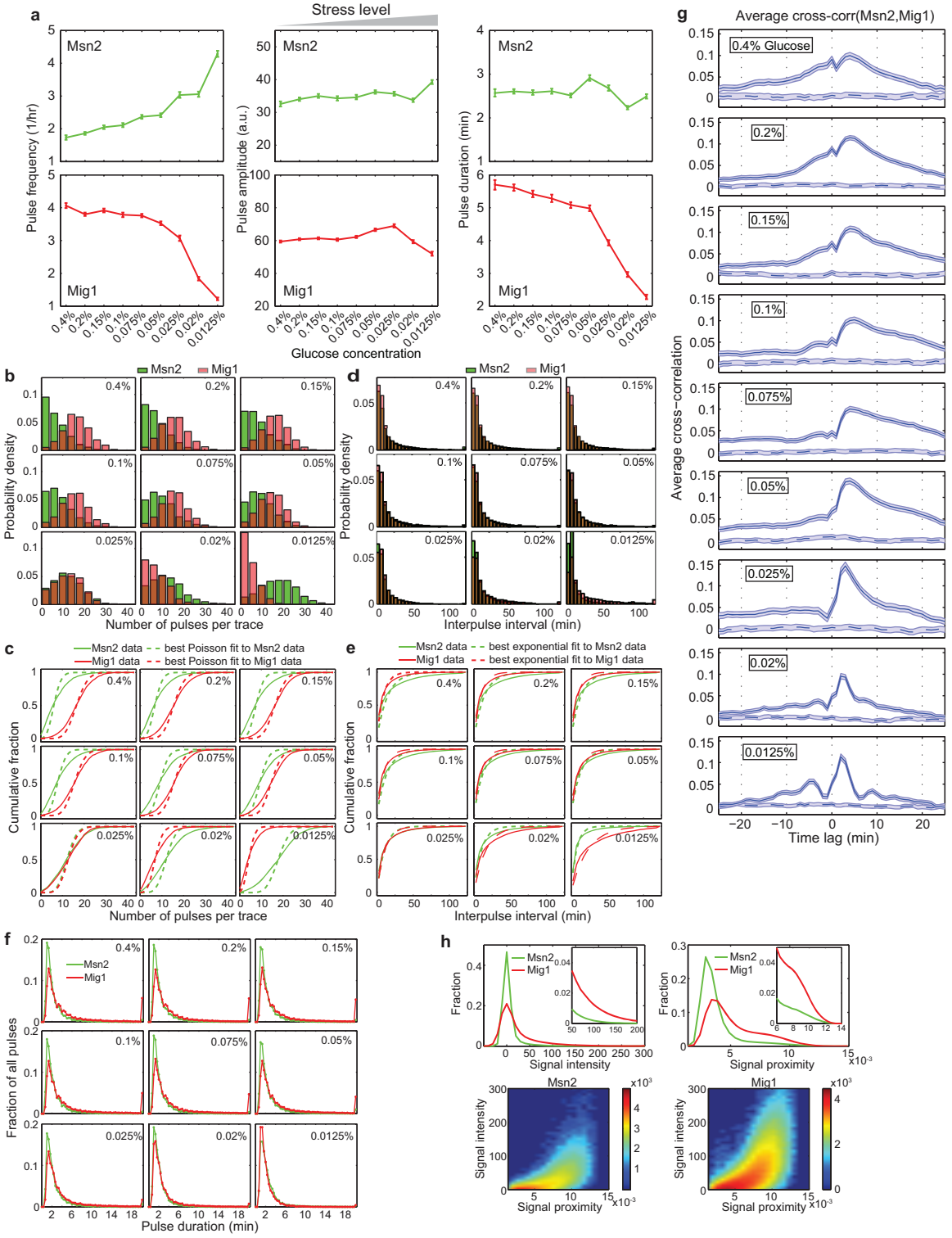

Extended Data Figure 7 | Characterization of Msn2 and Mig1 pulses and average cross-correlation functions between Msn2 and Mig1 in individual cells across different constant glucose concentrations. **a**, Pulse frequency, amplitude, and duration analysis. Single-cell traces at each glucose level were analysed and the mean frequency, amplitude and duration for both Msn2 and Mig1 were plotted. **b**, **c**, Distributions of total number of pulses per trace across glucose concentrations (**b**), along with corresponding fits to Poisson distributions (shown as cumulative distributions, **c**). Kolmogorov–Smirnov (KS) tests showed that these distributions differ significantly from Poisson distributions ($P < 10^{-16}$). **d**, **e**, Analogous plots for the distributions of inter-pulse time intervals (**d**), and corresponding fits to exponential distributions (**e**). These distributions differ significantly from exponential distributions according to KS tests ($P < 10^{-57}$). **f**, Distributions of pulse duration for Msn2 and Mig1 across glucose concentrations. **g**, Cross-correlation function (solid blue) of Msn2 and Mig1 nuclear localization traces, that is, cross-corr(Msn2, Mig1) (Methods). Dashed blue lines represent negative (independent) controls, calculated by scrambling the Msn2-Mig1 trace pairs within a population of cells (that is, cross-correlating Msn2 from one cell with Mig1 from another, randomly chosen, cell). Shading and error bars indicate 95% confidence intervals of the mean. The number of cells analysed in each glucose concentration: 1,511 (0.4%), 3,475 (0.2%), 2,605 (0.15%), 2,075 (0.1%), 3,034 (0.075%), 2,768 (0.05%), 1,392 (0.025%), 2,055 (0.02%), and 1,906 (0.0125%). **h**, Two different localization metrics show similar Msn2 and Mig1 state distributions. Top left, histogram of the intensity score for Msn2 and Mig1 shows long-tailed distributions for both proteins with peaks around zero (basal state). Insert, zoomed-in view of the tails. Top right, analogous plots for the signal proximity score also show long-tailed distributions with clear basal states. Signal proximity is the inverse of the distance-based localization metric described in the Methods section. High signal proximity indicates that the top 10 brightest pixels in the cell are close to each other. (Bottom) Signal intensity positively correlates with signal proximity for both Msn2 and Mig1, suggesting that these two independent scores show related features. This data are for cells at 0.05% glucose. Similar behaviours are observed across other glucose concentrations.

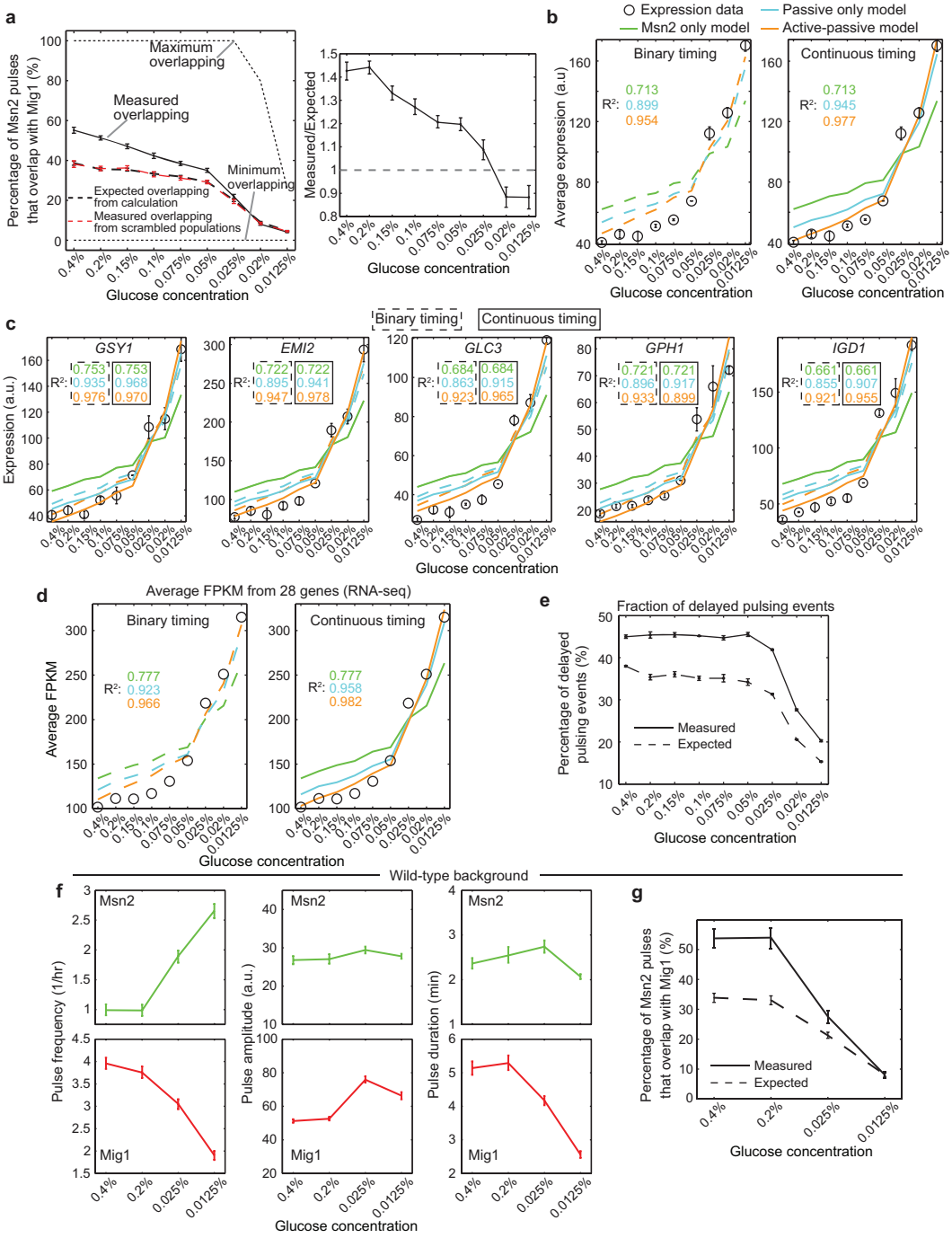

Extended Data Figure 8 | Further characterization of relative pulse timing modulation under steady-state conditions. **a**, Left, experimentally measured overlapping fraction (solid black) can be compared to minimum and maximum possible overlapping fractions (bottom and top dashed lines, respectively). The expected overlapping fraction for independent Msn2 and Mig1 dynamics is determined two ways: either computed from the Mig1 duty cycle (dashed black), or measured from scrambled populations (dashed red). Minimum and maximum possible fractions were calculated with the measured duty cycles of Msn2 and Mig1 pulses. Right, the ratios of measured overlapping fraction to expected overlapping fraction across glucose concentrations. **b**, Relative pulse timing modulation explains gene-expression dependence on glucose level for combinatorial target promoters. Black circles represent mean expression of 5 genes measured by qPCR (see Methods for normalization). Data were fit with three models, as indicated. See Methods and Supplementary Discussion for more details on binary and continuous timing models. R^2 values for fits are indicated in corresponding colours. Error bars indicate s.e.m. calculated from 3 biological replicates. **c**, Expression data for the 5 individual genes fit to the binary timing (dashed lines; R^2 values in dashed box) as well as continuous timing (solid lines; R^2 values in solid box) models. **d**, Analysis of RNA-seq expression data across 9 glucose concentrations. The averaged expression levels from 28 of the 31 identified combinatorial targets (Extended Data Fig. 2f–k) were fit with the binary or continuous timing modulation models (left and right plots, respectively). Three genes were excluded because they did not display a monotonic dependence on glucose (*YER067C-A*, *YKR098C*, *YLR109W*). In this analysis, parameter b was independently estimated from an *msn2* mutant at 0.2% glucose (samples collected on the same day). **e**, Glucose level modulates the fraction of delayed pulse timing events (see also Extended Data Fig. 4 and Supplementary Discussion). Total fractions of delayed overlapping (see Extended Data Fig. 4e, left) and delayed non-overlapping pulse events (see Extended Data Fig. 4f, left) were plotted across glucose concentrations. Expected fractions were computed from 'scrambled' populations where Msn2 and Mig1 dynamics are, by construction, independent. **f**, **g**, Glucose concentration also modulates relative pulse timing in a control strain without deletions of *msn4* and *mig2*. **f**, Pulse characteristics of both Msn2 and Mig1 for varying glucose concentrations. **g**, Measured versus expected overlapping fractions across different glucose concentrations (see **a**) for the wild-type background that was not deleted for Msn4 and Mig2. Error bars indicate 95% confidence intervals of the mean (except for **b**–**d**). The number of cells analysed for **f**, **g**: 618 (0.4%), 541 (0.2%), 714 (0.025%), and 775 (0.0125%).

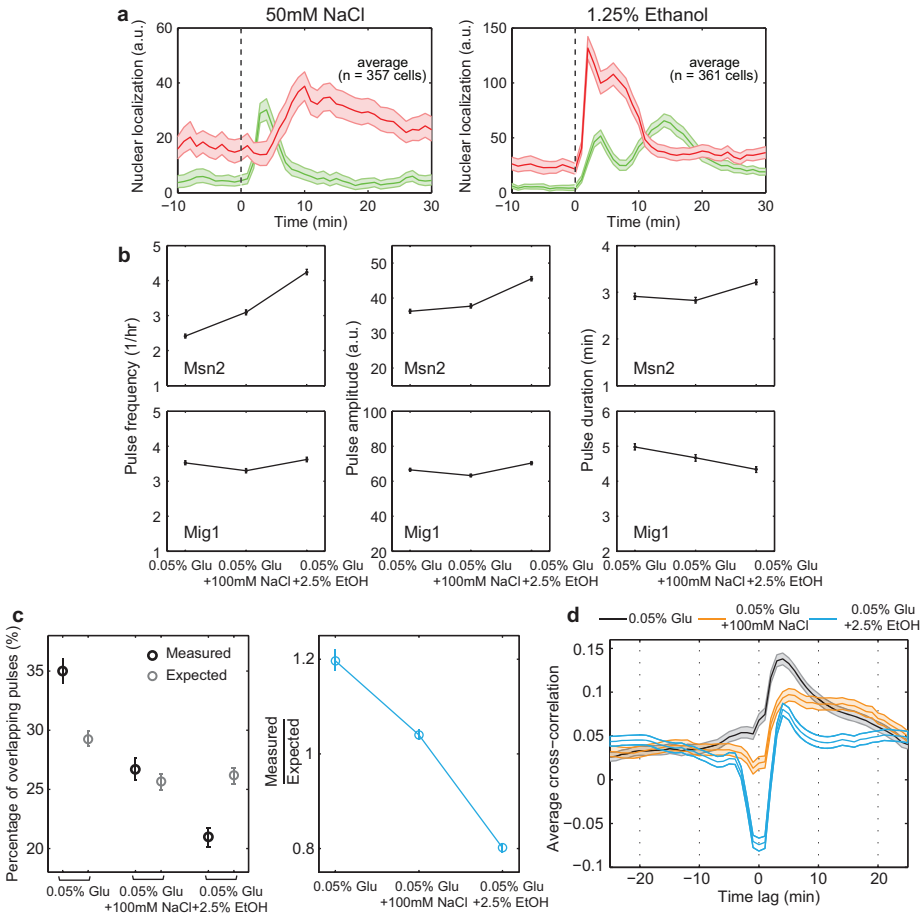

Extended Data Figure 9 | Additional effects of stress level and type on transient and steady-state responses. **a**, Stress level does not modulate relative pulse timing during transient responses. Averaged nuclear localization traces of Msn2–mKO2 and Mig1–mCherry during transient response to 50 mM NaCl (left) or 1.25% ethanol (right) are shown (see Fig. 2b, c). **b**, Additional stresses modulate relative timing during steady-state responses. Changes in pulse characteristics of both Msn2 and Mig1 in response to the addition of 100 mM NaCl or 2.5% ethanol during steady-state growth at 0.05% glucose. **c**, Measured (black) versus expected (grey) overlapping fractions for the same 3 conditions as in **b**. **d**, Averaged cross-correlation between Msn2 and Mig1 time traces for the same three conditions. See Supplementary Discussion for additional discussion. Shading and error bars indicate 95% confidence intervals of the mean. The number of cells analysed for **b**, **d**: 2,768 (0.05% glucose), 2,178 (0.05% glucose with 100 mM NaCl) and 2,115 (0.05% glucose with 2.5% ethanol).

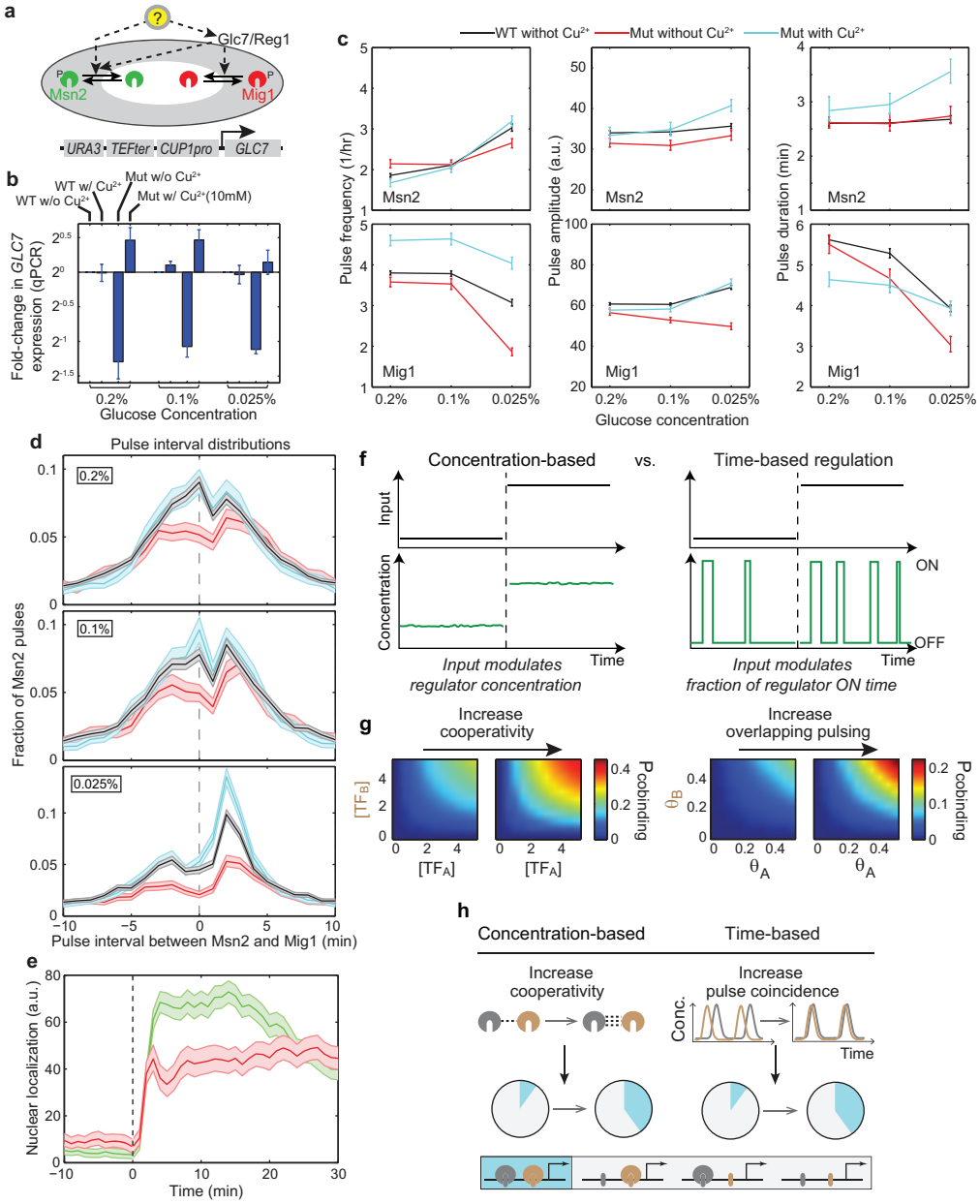

Extended Data Figure 10 | A role for Glc7 in active relative pulse timing modulation under constant glucose conditions and functional aspect of relative pulse timing modulation. **a**, Schematic of potential mechanisms for Glc7-dependent relative pulse timing modulation (top) and construct design (bottom). Overlapping pulsing of Msn2 and Mig1 could be induced by either a common kinase/phosphatase (such as Glc7) that directly or indirectly activates both Msn2 and Mig1 localization, or by an upstream input (yellow circle) that simultaneously regulates kinases/phosphatases responsible for Msn2 and Mig1 localization. To analyse the role of *GLC7* in relative pulse timing, we constructed a strain in which the normal *GLC7* promoter is replaced by a copper-inducible promoter, as shown. **b**, qPCR characterization of the inducible *GLC7* strain across three glucose concentrations. Basal copper level in the media reduced *GLC7* expression to less than 50% of its wild-type level. Addition of 10 μM $CuSO_4$ restored the expression to 110% to 140% of wild-type level. **c**, Changes in pulse characteristics in response to *GLC7* reduction (red) and restoration (blue), compared to wild-type (black). **d**, Corresponding changes in pulse interval distribution. Pulse interval was calculated as the distance between the peak of a given Msn2 pulse and the peak of its closest Mig1 pulse within a 21 min window. **e**, Averaged nuclear localization traces of Msn2–mKO2 (green) and Mig1–mCherry (red) in response to 2.5% ethanol addition (dashed line) for the *GLC7* reduction mutant. See Supplementary Discussion for additional discussion. Error bars in **b** indicate s.e.m. from 3 biological replicates. For **c**–**e**, shading and error bars indicate 95% confidence intervals of the mean. The number of cells analysed in the mutant strain: 671 (0.2% glucose without Cu^{2+}), 540 (0.1% glucose without Cu^{2+}), 719 (0.025% glucose without Cu^{2+}), 756 (0.2% glucose with Cu^{2+}), 643 (0.1% glucose with Cu^{2+}), and 656 (0.025% glucose with Cu^{2+}). **f**–**h**, Functional aspect of relative pulse timing modulation (see Supplementary Note). **f**, Concentration-based versus time-based regulation. Input modulates the regulator concentration (left) versus the fraction of regulator ON time (right). **g**, Modulation of relative pulse timing in time-based regulation results in changes in the effective protein–protein cooperativity. Increasing protein–protein cooperativity in concentration-based regulation changes the probability of co-binding of TF_A and TF_B (left). Increasing overlapping pulsing in time-based regulation leads to qualitatively similar changes in the probability of co-binding (right). Protein cooperativity parameter ω_{AB} was increased from 1 to 2 for the left plots. Overlap fraction was increased from $\theta_A\theta_B$ to $2 \times \theta_A\theta_B$ for the right plots ($\omega_{AB} = 1$). $K_A = K_B = 5$ for both left and right. **h**, Schematic, relative pulse timing modulation affects the relative probability of simultaneous binding of two transcription factors to a target promoter (right). This effect is analogous to that generated by cooperative protein–protein interactions (left)[44]. Stronger protein–protein interactions or a higher overlap fraction can both increase the probability with which two transcription factors will be simultaneously bound at neighbouring sites (schematic pie charts).